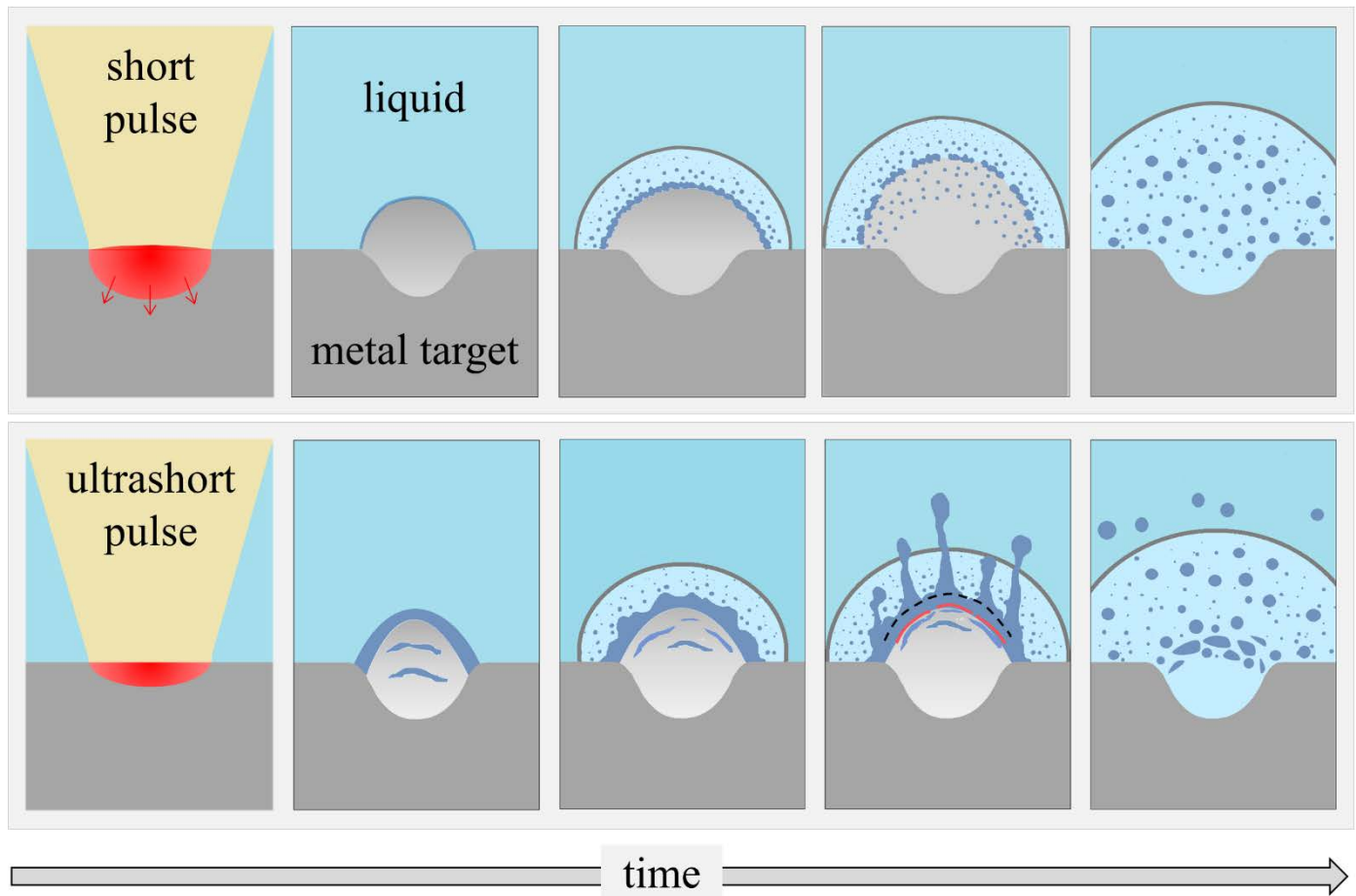# The effect of pulse duration on nanoparticle generation in pulsed laser ablation in liquids: Insights from large-scale atomistic simulations

Cheng-Yu Shih,[1,2] Maxim V. Shugaev,[1] Chengping Wu,[1] and Leonid V. Zhigilei[1]

[1] Department of Materials Science and Engineering, University of Virginia, 395 McCormick Road, Charlottesville, Virginia 22904-4745, USA

[2] Longterm Concept International Pte Ltd, 111 North Bridge Road #18-01, Peninsula Plaza, Singapore, 179098

The effect of the laser pulse duration on the nanoparticle generation in laser ablation in liquids is investigated. Three mechanisms operating at different stages of the ablation process and in different parts of the cavitation bubble are identified.

The effect of pulse duration on nanoparticle generation in pulsed laser ablation in liquids: insights from large-scale atomistic simulations†

Cheng-Yu Shih,[ab] Maxim V. Shugaev, [ID][a] Chengping Wu[a] and Leonid V. Zhigilei [ID] *[a]

The generation of colloidal solutions of chemically clean nanoparticles through pulsed laser ablation in liquids (PLAL) has evolved into a thriving research field that impacts industrial applications. The complexity and multiscale nature of PLAL make it difficult to untangle the various processes involved in the generation of nanoparticles and establish the dependence of nanoparticle yield and size distribution on the irradiation parameters. Large-scale atomistic simulations have yielded important insights into the fundamental mechanisms of ultrashort (femtoseconds to tens of picoseconds) PLAL and provided a plausible explanation of the origin of the experimentally observed bimodal nanoparticle size distributions. In this paper, we extend the atomistic simulations to short (hundreds of picoseconds to nanoseconds) laser pulses and focus our attention on the effect of the pulse duration on the mechanisms responsible for the generation of nanoparticles at the initial dynamic stage of laser ablation. Three distinct nanoparticle generation mechanisms operating at different stages of the ablation process and in different parts of the emerging cavitation bubble are identified in the simulations. These mechanisms are (1) the formation of a thin transient metal layer at the interface between the ablation plume and water environment followed by its decomposition into large molten nanoparticles, (2) the nucleation, growth, and rapid cooling/solidification of small nanoparticles at the very front of the emerging cavitation bubble, above the transient interfacial metal layer, and (3) the spinodal decomposition of a part of the ablation plume located below the transient interfacial layer, leading to the formation of a large population of nanoparticles growing in a high-temperature environment through inter-particle collisions and coalescence. The coexistence of the three distinct mechanisms of the nanoparticle formation at the initial stage of the ablation process can be related to the broad nanoparticle size distributions commonly observed in nanosecond PLAL experiments. The strong dependence of the nanoparticle cooling and solidification rates on the location within the low-density metal–water mixing region has important implications for the long-term evolution of the nanoparticle size distribution, as well as for the ability to quench the nanoparticle growth or dope them by adding surface-active agents or doping elements to the liquid environment.

1. Introduction

The generation of chemically clean and environmentally friendly nanoparticles through pulsed laser ablation in liquids (PLAL) has a number of advantages over conventional chemical synthesis methods and has evolved into a thriving research field attracting laboratory and industrial applications.[1] The practical importance

of PLAL has stimulated extensive experimental and theoretical efforts aimed at revealing the effect of various parameters of PLAL on nanoparticle production efficiency and size distribution, *e.g.*, see recent reviews.[2–4] Laser pulse duration is recognized as one of the key parameters of PLAL that affects all aspects of the ablation process. The lifetime and size of the cavitation bubble,[5–8] the presence or absence of satellite microbubbles,[8–11] nanoparticle yield and size distribution[12–17] have all been shown to be sensitive to the laser pulse duration.

Since most of the applications of colloidal nanoparticles require narrow and tunable size distributions, a clear understanding of the effect of the pulse duration on the nanoparticle yield and size distribution is of particular interest. The complexity and multiscale nature of PLAL, however, make it difficult to

[a] *Department of Materials Science and Engineering, University of Virginia, 395 McCormick Road, Charlottesville, Virginia 22904-4745, USA. E-mail: lz2n@virginia.edu*

[b] *Longterm Concept International Pte Ltd, 111 North Bridge Road #18-01, Peninsula Plaza, 179098, Singapore*

This journal is © the Owner Societies 2020

*Phys. Chem. Chem. Phys.*, 2020, **22**, 7077–7099 | 7077

untangle the various processes involved in the generation of nanoparticles that can be sensitive to the pulse duration. For instance, two orders of magnitude increase in the yield of Au nanoparticles produced by PLAL in water was observed with an increase in the pulse duration from 150 fs to 2 ps.[13] This strong dependence was attributed to the nonlinear laser light absorption and photoionization of the liquid in the femtosecond irradiation regime. In contrast, a minimum of the nanoparticle yield was reported at a similar pulse duration of 3 ps in a study of near-threshold ablation of Au in water.[16] This observation was attributed to interfacial boiling of water,[16] but it could also be related to the attenuation of the laser light by nanoparticles accumulated in the solution above the laser spot under conditions of high repetition rate (0.5 MHz) irradiation used in this study.[3] Indeed, it has been demonstrated that the nanoparticle productivity can be drastically increased by performing ablation in a flow chamber, so that the nanoparticles and bubbles are effectively removed from the path of the laser beam.[12,18]

Beyond the effects related to the laser light propagation through the liquid environment, the pulse duration is defining the rate and spatial extent of the laser energy deposition in the target and, as a result, the initial dynamics of the ablation process. The initial material response to the laser energy deposition, however, is largely inaccessible to experimental probing[5–11,19–23] and remains poorly understood. It is tempting to extend the concepts and physical intuition from the much better explored nanoparticle generation by laser ablation in vacuum and in a background gas to PLAL.[3,16,24–26] It is generally accepted that the primary mechanism of nanoparticle formation in laser ablation in vacuum is a process commonly referred to as "phase explosion" or "explosive boiling".[27–30] In this process, a surface region of the irradiated target is superheated above the limit of thermodynamic stability of the liquid phase and undergoes a rapid decomposition into a mixture of vapor and liquid droplets. The results of large-scale molecular dynamics (MD) simulations suggest that the phase explosion proceeds through the formation of a foamy transient structure of interconnected liquid regions and produces droplets and atomic clusters of different sizes.[31,32] For pulse durations shorter than the time needed for mechanical equilibration of the absorbing volume (a few tens of picoseconds for metals), the condition of stress confinement[33,34] is satisfied, strong thermoelastic stresses are generated, and the relaxation of these stresses can cause subsurface cavitation[35] and ejection of large liquid droplets.[28,32] The contribution of thermoelastic stresses not only reduces the ablation threshold but can also significantly increase the ablation yield and the fraction of large droplets in the ejected plume at laser fluences above the threshold for the onset of the phase explosion.[28,30] When the pulse duration is extended beyond the conditions of stress confinement and into the nanosecond regime, the fraction of vapor phase in the ablation plume gradually increases, even though the phase explosion, and the associated generation of liquid droplets, can still take place for laser pulses much longer than hundreds of nanoseconds.[36,37] Finally, the expulsion of large liquid droplets can be driven by the ablation recoil pressure gradient[38,39] even under continuous wave (CW) laser irradiation with a sufficiently high power.

While well-developed, the fundamental knowledge on laser-metal interactions in vacuum cannot be directly applied to PLAL. The results of recent MD simulations of PLAL performed for Ag in water in the irradiation regime of stress confinement (laser pulses of ∼10 ps and shorter, referred to in this paper as ultrashort)[8,40–42] demonstrate that the generation of nanoparticles in PLAL is a complex multistep phenomenon where the interaction of the ejected material with the liquid environment plays the dominant role. The sequence of dynamic processes responsible for the nanoparticle generation, revealed in the simulations, is illustrated in Fig. 1 and is briefly summarized below.

The initial material response to the laser energy deposition is similar to that in laser ablation in vacuum, i.e., the electrons excited by the laser irradiation thermalize with atomic vibrations on the timescale defined by the strength of electron–phonon coupling (a few picoseconds to tens of picoseconds), leading to rapid heating, melting, and explosive decomposition of a
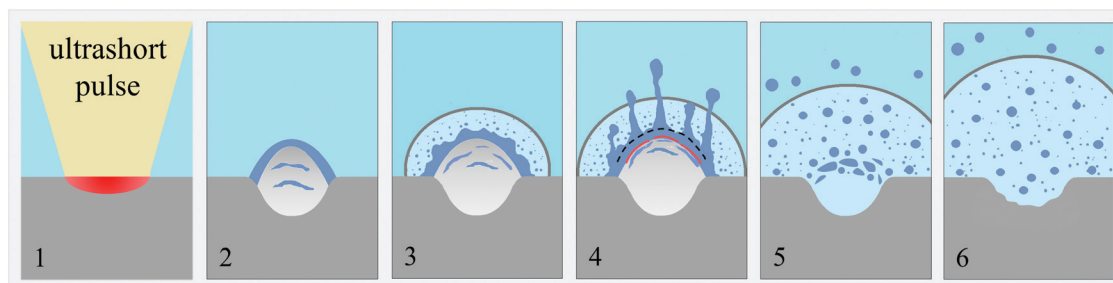
Fig. 1 Schematic illustration of the sequence of dynamic processes triggered by irradiation of a metal target by an *ultrashort (femtosecond to tens of picosecond) laser pulse*. The liquid water is colored blue, the metal target is grey, the ablation plume is light grey, and the expanding cavitation bubble is light blue. The metal nanoparticles and a transient molten metal layer generated at the plume–water interface are shown in dark blue color. The red curves in panel 4 show schematically the backside impacts from large (spalled) metal droplets joining the hot molten metal layer formed at the ablation plume–water interface. The impacts generate pressure pulses (shown by dashed curves) that induce jetting of the molten metal (Richtmyer–Meshkov instability) from the layer roughened by Rayleigh–Taylor instability of the plume–water interface. The schematic is informed by large-scale atomistic simulations reported in ref. 8, 40 and 41.

surface region of the target into vapor and liquid regions. The rapid release of vapor combined with the relaxation of thermo-elastic stresses generated under conditions of stress confinement drives the ejection of the hot mixture of vapor and liquid regions from the target. In contrast to the ablation in vacuum, the ablation plume cannot expand freely but is rapidly decelerated by the water environment. The deceleration leads to the accumulation of the ablation plume at the interface with water and formation of a hot metal layer (panel 2 in Fig. 1). The water in contact with the metal layer is brought to the supercritical state, expands, and absorbs metal atoms emitted/vaporized from the hot metal layer. The expanding low-density metal–water mixing region provides an environment suitable for rapid nucleation and growth of small metal nanoparticles and serves as a precursor to the formation of a cavitation bubble (panel 3 in Fig. 1). The rapid deceleration of the higher density metal layer by the lighter supercritical water creates classical conditions for the development of Rayleigh–Taylor instability[43] at the decelerated interface. The large magnitude of the deceleration at the initial stage of the plume expansion, on the order of 10^{12} m s^{-2}, brings the characteristic length and time scales of the interface roughening due to the Rayleigh–Taylor instability down to tens of nanometers and hundreds of picoseconds.[41] The thin hot metal layer roughened by the Rayleigh–Taylor instability has limited stability and can readily disintegrate into large (tens to hundreds of nanometers) nanoparticles. Moreover, the backside impacts from large metal droplets ejected with the assistance of photomechanical processes and joining the hot molten metal layer at a later time can induce pressure pulses in the layer that are sufficiently strong to cause jetting and injection of metal droplets directly into the high-density water region located above the low-density mixing region[8,41] (panel 4 in Fig. 1). As discussed in ref. 41, the jetting can be attributed to Richtmyer–Meshkov instability that occurs when a pressure pulse impinges a rough interface between two fluids of different density.[44] The two fluids are the heavier metal layer and lighter supercritical water, and the interface is roughened by the Rayleigh–Taylor instability emerging during the ablation plume deceleration by the water environment, as discussed above.

The two distinct mechanisms of the nanoparticle formation, the rapid nucleation and growth of small nanoparticles in the metal–water mixing region and the breakup of the hot metal layer into larger droplets due to the hydrodynamic instabilities (panels 5 and 6 in Fig. 1), yield nanoparticles of two different size ranges as early as several nanoseconds after the laser irradiation. This computational result provides a plausible explanation for the experimental observations of bimodal nanoparticle size distributions in femtosecond and picosecond PLAL experiments.[8,45–48] Moreover, the injection of large nanoparticles into water beyond the cavitation bubble boundary, predicted in the simulations, is confirmed in recent double-pulse cavitation bubble imaging experiments,[8] as well as in time-resolved X-ray probing of the size and crystallinity of nanoparticles present in the expanding cavitation bubble.[19] In agreement with the computational predictions, the latter

study confirms that large nanoparticles are present already at the advancing front of the bubble, and the first particles are detected even before the bubble front reaches the level of the probe beam. The rapid cooling and crystallization of the liquid droplets injected into the dense water environment above the cavitation bubble boundary are observed in the simulations[8,41] and, indeed, the largest crystalline domains are detected for nanoparticles located outside the cavitation bubble in the experiments.[19] A recent computational study[42] also reveals that a prompt disintegration of the dense metal layer formed at the plume–water interface can be assisted by the lateral pressure gradients created by spatially modulated laser energy deposition, thus suggesting a possible method for suppressing the generation of the largest nanoparticles and minimizing the material waste in the nanoparticle generation by PLAL.

The multistep physical picture of the nanoparticle formation discussed above for ultrashort pulse (femtosecond and picosecond) laser ablation in liquids is likely to change when the pulse duration is increased to hundreds of picoseconds or nanoseconds. Indeed, the nanoparticle size distributions in nanosecond PLAL tend to be narrower,[49] and the separation into two modes of the bimodal size distributions is less pronounced. Nevertheless, the coexistence of small (several to tens of nanometers) and large (tens to hundreds of nanometers) nanoparticles is still observed in nanosecond PLAL experiments,[21,25,50,51] and the large nanoparticles can make up a substantial fraction of the mass-weighted nanoparticle size distribution.[52] The two subgroups of nanoparticles have also been identified in time-resolved small-angle X-ray scattering (SAXS) probing of cavitation bubbles generated in nanosecond PLAL.[6,20–23] The two groups are commonly described as "primary" and "secondary" nanoparticles, implying a sequential generation of the secondary nanoparticles through collisions and agglomeration of the primary ones,[6,20] with the latter assumed to form through the condensation from the vapor phase at the initial stage of the cavitation bubble expansion. More recent SAXS probing of the cavitation bubble interior,[21] however, suggests that at least some of the large nanoparticles are already present inside the expanding cavitation bubble, where they coexist with the smaller nanoparticles. These observations are consistent with the results of MD simulations discussed above, which suggest that alternative scenarios of the large/secondary nanoparticle generation may already be realized at the early stage of the ablation process. The applicability of the computational predictions obtained in the simulations of femtosecond/picosecond PLAL to longer pulses, however, is questionable and should be tested in additional simulations.

In this paper, we extend the MD simulations to longer (hundreds of picoseconds and nanoseconds) laser pulses and focus our attention on the mechanisms responsible for the generation of nanoparticles at the initial dynamic stage of laser ablation. By relating results of these simulations to the physical picture reviewed above for the ultrashort (up to tens of picoseconds) laser pulses, the possible origins of the

This journal is © the Owner Societies 2020

Phys. Chem. Chem. Phys., 2020, **22**, 7077–7099 | **7079**

dependence of the nanoparticle size distribution on laser pulse duration are discussed.

2. Computational setup

The simulations reported in this paper are performed for a bulk Ag target covered by water and irradiated by 400 ps, 1 ns, and 2 ns laser pulses. A model combining a fully atomistic description of laser interaction with the metal target,[30,32,53,54] a coarse-grained representation of the water environment,[40,55,56] and acoustic impedance matching boundary conditions designed to mimic the nonreflecting propagation of the laser-induced pressure waves through the boundaries of the computational domain[57] is used in the simulations. To facilitate the comparison with earlier results obtained for shorter, 100 fs and 10 ps, laser pulses,[8,41] the same computational setup is used in the present study. Since a complete description of the combined model is provided in ref. 8, 40 and 41, only a brief description of the model and the computational setup is provided below.

A schematic representation of the computational system is shown in Fig. 2. The laser interaction with a bulk Ag target is simulated with an atomistic MD model combined with a continuum-level description of laser excitation of conduction band electrons followed by electron–phonon equilibration based on two-temperature model (TTM).[58] The combined TTM-MD model is described in earlier publications,[30,32,53] and the parameters of the model used in the simulations of laser interaction with Ag are provided in ref. 8, 40, 41 and 54. Briefly, the description of the electron temperature dependences of the electron–phonon coupling factor and electron heat capacity of Ag included in the TTM equation accounts for the thermal excitation from the electron states below the Fermi level.[59] The temperature dependence of the electron thermal conductivity is described by the Drude model relation with the electron–electron and electron–phonon scattering rates estimated within the free electron model and fitted to the experimental values of thermal conductivity of solid Ag at the melting temperature.[54] The expansion, density variation, and disintegration of the irradiated target predicted in the MD part of the model are accounted for through the corresponding changes of the parameters of the TTM equation for electron temperature.

The liquid environment is represented by a combination of a coarse-grained (CG) MD model[40,55,56] used in the vicinity of the irradiated target with a non-reflecting boundary condition[57] (NRB-w in Fig. 2). The boundary condition is parametrized to simulate a non-reflecting propagation of the pressure wave generated by laser ablation of the Ag target from the CG water region into the overlying semi-infinite water environment. In the CG MD model, each particle represents several water molecules, and the degrees of freedom missing in such CG representation of water are accounted for through a heat bath approach that associates an internal energy variable with each CG particle.[40,55,56] The CG model is fitted to exactly
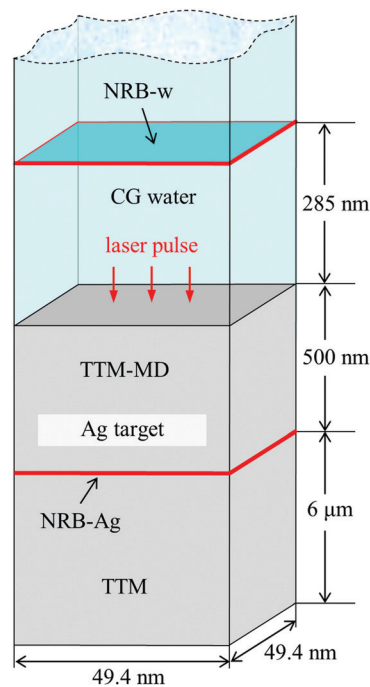

Fig. 2 Schematic representation of the initial system used in simulations of short pulse laser interaction with a bulk Ag target in water. The top part of the Ag target (shown by grey color) is represented by TTM-MD model, whereas the temperature evolution in the deeper part of the target is described by TTM equations. A 285 nm-thick layer of water adjacent to the metal target is represented by a coarse-grained MD model (CG water). At the bottom of the TTM-MD domain and on the top of the CG water region, the non-reflecting propagation of the laser-induced pressure waves is reproduced by acoustic impedance matching boundary conditions denoted as NRB-Ag and NRB-w, respectively. In the lateral directions, parallel to the irradiated surface, periodic boundary conditions are applied. The dimensions of the computational system marked on the schematic are used in the simulation of 400 ps pulse laser irradiation discussed in Sections 3.1 and 3.2. A smaller system with lateral dimensions of 4.94 nm × 4.94 nm is used in the simulations performed for longer pulse durations of 1 and 2 ns and reported in Section 3.3.

reproduce the density and heat capacity of water, while other properties relevant to the simulation of laser ablation in water, such as speed of sound, bulk modulus, viscosity, surface energy, melting temperature, critical temperature, and critical density, do not deviate from the experimental values by more than 25%.[40,55]

The interatomic interactions in the TTM-MD part of the model are described by the embedded atom method (EAM) potential with the functional form and parameterization developed in ref. 60. Although this potential is originally fitted to low-temperature values of the equilibrium lattice constant, sublimation energy, elastic constants, and vacancy formation energy, it also provides an adequate description of high temperature thermodynamic properties of Ag relevant to the simulation of laser-induced processes.[40,41,54,57,61,62] In particular, the equilibrium melting temperature, T_m, determined in liquid-crystal coexistence MD simulations is found to be 1139 K,[62] about 8% below the experimental value of 1235 K.[63] The critical temperature is roughly estimated to be in the range of 3500–4500 K based on the conditions for the onset

7080 | *Phys. Chem. Chem. Phys.*, 2020, **22**, 7077–7099

This journal is © the Owner Societies 2020

of the phase explosion in small-scale MD simulations.[57] In the present work we perform a more accurate evaluation of the liquid–vapor binodal, critical point, and surface tension of the model EAM Ag, with the results provided in the Appendix.

The atomistic TTM-MD representation is used only in the top 500 nm-deep part of the metal target, where the laser-induced phase transformations take place. In the deeper part of the target, beyond the TTM-MD region, the electron heat conduction and the energy exchange between the electrons and the lattice are described by the conventional TTM equations. The TTM part of the model extends 6.5 μm down from the irradiated surface of the Ag target to ensure the absence of any significant increase in the electron or lattice temperatures at the bottom of the computational domain by the end of the simulation. At the boundary between the TTM-MD and TTM parts of the model, another acoustic impedance matching boundary condition designed to mimic a non-reflecting propagation of the laser-induced pressure wave into the bulk of the Ag target (NRB-Ag in Fig. 2) is applied. The NRB-w and NRB-Ag boundary conditions implicitly simulate a liquid overlayer and a metal target that are sufficiently thick, so that the reflections of laser-induced pressure waves from the free surface of the liquid overlayer and the back side of the bulk metal target do not play any role in the generation of nanoparticles.

The computational system represents a small region within the laser spot, and periodic boundary conditions are applied in the lateral directions, parallel to the surface of the target. In the simulation discussed in Sections 3.1 and 3.2, where 400 ps laser pulse is used, the lateral dimensions of the computational system are 49.4 nm × 49.4 nm. With a 500 nm-deep part of the Ag target represented with atomic resolution and a 285 nm-thick part of the water environment represented by CG MD, the model includes 70 million Ag atoms and 8.5 million CG particles. The relatively large number of atoms/particles in the computational system and the need to follow the evolution of the system for as long as 8 ns make the computational cost of the simulation rather high and prevent us from running multiple simulations for different irradiation conditions. Therefore, a much smaller computational system with lateral dimensions of 4.94 nm × 4.94 nm (699 840 Ag atoms and 84 868 CG water particles) is used in three additional simulations reported in Section 3.3 and performed for longer pulse durations of 1 and 2 ns. In this case, the small lateral size of the computational system prevents us from any meaningful analysis of the nanoparticle formation or size distributions. Nevertheless, these small-scale simulations still provide some useful complementary information on the thermodynamic conditions realized in nanosecond PLAL. All systems used in the simulations are thoroughly equilibrated at 300 K before applying the laser irradiation.

The energy deposition by a laser pulse is simulated through a source term added to the TTM equation for the electron temperature.[53] The source term simulates the excitation of the conduction-band electrons by a laser pulse with a Gaussian temporal profile and reproduces the exponential attenuation of laser intensity with depth under the surface (Beer–Lambert law). The effective depth of the laser energy deposition used

in the source term includes the optical penetration depth and the effective depth of the "ballistic" energy transport before the thermalization of the excited electrons.[8,41,54] The implementation of the source term is based on a cell-by-cell attenuation of the laser light to allow for the laser energy deposition into the surface region of the target undergoing expansion during the laser pulse. The mass absorption coefficient is considered to be constant, i.e., when the material expands, the local linear absorption coefficient decreases according to the local changes of the material density. Given the dominant role of the thermal conduction in defining the energy and temperature profiles produced in the surface region of the irradiated target by laser pulses longer than a hundred of picoseconds, this approach to the laser energy deposition is unlikely to introduce any significant artifacts to the results of the simulations. To ensure complete deposition of the laser pulse energy to the target, the maximum of the Gaussian temporal profile is shifted with respect to the start of the simulation (zero time) by $2.5\tau_p$, where τ_p is the laser pulse duration defined as the full width at half-maximum of the Gaussian profile.

The conversion of the absorbed laser fluence used in the simulations to the incident laser fluence, usually reported in experimental studies, becomes less straightforward as compared to ultrashort pulses, where the electron temperature dependence of the reflectivity and optical absorption coefficient can be evaluated theoretically[8,64] by neglecting the material expansion and the onset of density fluctuations during the laser pulse. While the prompt material decomposition into vapor, small atomic clusters and droplets is suppressed in PLAL due to the ablation plume confinement by the liquid environment, the density fluctuations and nucleation of first atomic clusters at the Ag–water interface are still observed at the tails of the Gaussian temporal profiles of 1 ns and 2 ns laser pulses (see Fig. 11). A realistic modeling of the laser interaction with superheated material that is just starting to undergo phase decomposition and cannot yet be represented as a mixture of well-defined individual components (atoms, ions, electrons, atomic clusters and spherical droplets) is far from being straightforward and is beyond the scopes of this paper. For the pulse duration of 400 ps, however, the relatively high density of the front part of the ablation plume and the retention of the fairly sharp plume–water interface during the pulse duration (e.g., see the Ag density profile for 1.4 ns in Fig. 3c and note that the laser intensity peaks at 1 ns for this pulse duration) support the validity of the simplified treatment of the laser energy deposition used in the simulations.

3. Results and discussion

The dependence of the nanoparticle generation mechanisms in PLAL on the laser pulse duration is explored in this work based on the results of four atomistic simulations. The general picture of PLAL and the evolution of thermodynamic parameters during the ablation process are discussed first, in Section 3.1, based on the results of a large-scale simulation of

This journal is © the Owner Societies 2020

Phys. Chem. Chem. Phys., 2020, 22, 7077–7099 | 7081
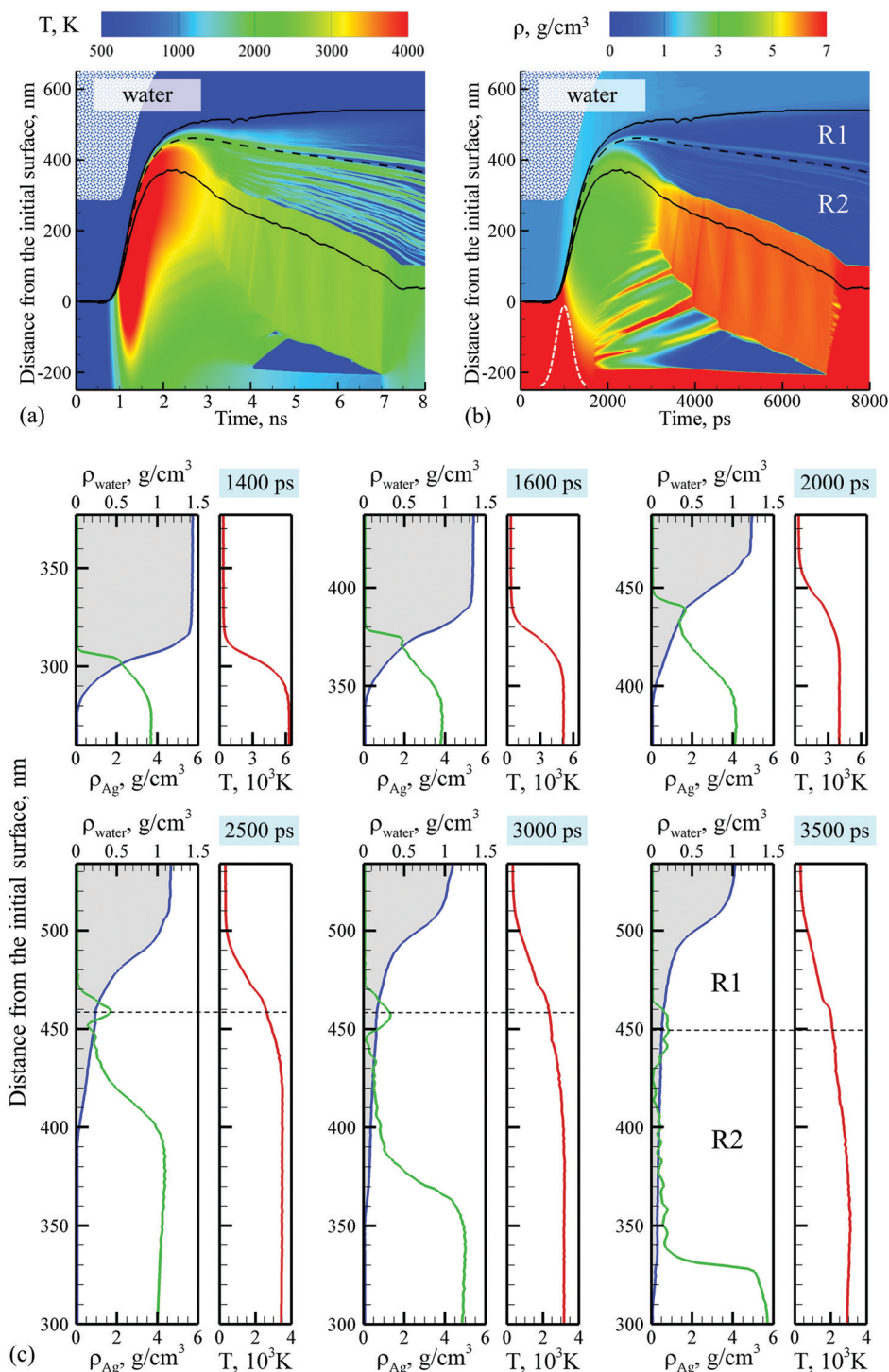
Fig. 3 The density and temperature evolution predicted in a large-scale atomistic simulation of a bulk Ag target irradiated in water by a 400 ps laser pulse at an absorbed fluence of 600 mJ cm^{-2}. The irradiation conditions correspond to the regime of phase explosion confined by the water environment. The density and temperature distributions are presented in the form of contour plots (a and b) and profiles plotted for several moments of time and focused on the expanding ablation plume−water mixing region (c). In the contour plots, two black lines outline the water−Ag mixing region defined as a region where both water molecules and Ag atoms are present. The blue dotted background in (a and b) represents the implicit presence of water beyond the pressure-transmitting boundary (NRB-w in Fig. 2) applied at the top of the water layer explicitly simulated with coarse-grained MD. The black dashed lines in (a and b) mark the approximate trajectory of the transient dense layer generated at the plume−water interface and the averaged position of large nanoparticles originating from this layer. This dashed line separates two parts of the ablation plume−water mixing region (marked as R1 and R2 in the density contour plot) where different kinetics of the nanoparticle formation is observed. The temporal shape of the Gaussian laser pulse is shown in the density contour plot by the white dashed curve. In (c), the density profiles are shown by blue lines outlining grey areas for water and by green lines for Ag. The corresponding temperature profiles are shown by red curves. The levels of the horizontal dashed lines crossing the profiles shown for 2500, 3000, and 3500 ps correspond to the locations of the dashed line separating regions R1 and R2 in the contour plots.

a bulk Ag target irradiated in water by a 400 ps laser pulse at an absorbed fluence of 600 mJ cm^{-2}. The value of laser fluence is chosen to be the same as the one used in a simulation of PLAL of Ag by a shorter 10 ps laser pulse reported in ref. 8, thus allowing for direct comparison of the computational predictions for the two pulse durations. The distinct nanoparticle generation mechanisms identified in different parts of the emerging cavitation bubble are discussed in Section 3.2. Finally, in Section 3.3, the effect of further increase of the laser pulse duration is explored in three smaller-scale simulations performed with 1 ns and 2 ns laser pulses.

3.1. Microscopic picture and mechanisms of ablation plume–water interaction

The simulation discussed in this section is performed for a Ag bulk target irradiated in water by a 400 ps laser pulse at an absorbed fluence of 600 mJ cm^{-2}. These irradiation conditions correspond to the regime of phase explosion discussed in the introduction, and the absorbed fluence is about three times higher than the threshold fluence for the onset of the phase explosion.[41] The temperature and density evolution during the ablation process, illustrated in Fig. 3, as well as the visual picture of the ablation plume interaction with water environment provided by atomistic snapshots in Fig. 4, exhibit both similar and distinct characteristics to those reported earlier for the same absorbed fluence but shorter, 10 ps, laser pulse.[8] Similar to the ablation by the shorter pulse, the ablation plume produced by the phase explosion of a superheated surface region of the irradiated target is attempting to expand but is rapidly decelerated by the water environment, leading to accumulation of the hot front part of the plume at the interface with water. The "vigor" of the plume expansion and, as a result, the density of the hot metal layer formed at the plume–water interface, however, are substantially reduced in ablation by the longer 400 ps pulse. Indeed, as can be seen from Fig. 3 and similar density plots in ref. 8, the plume front density at the end of the deceleration stage (~ 2 ns) is ~ 2–4 g cm^{-3} in the simulation performed with 400 ps laser pulse (Fig. 3), while it reaches ~ 6 g cm^{-3} under irradiation by the shorter, 10 ps, laser pulse.[8] Moreover, the jetting of hot molten metal into the dense water environment beyond the boundary of the emerging cavitation bubble, observed for shorter laser pulses and attributed to the sequential occurrence of Rayleigh–Taylor and Richtmyer–Meshkov instabilities at the plume–water interface,[8,41] is absent in the case of the longer pulse. Instead, the top part of the ablation plume in contact with water environment decomposes into large droplets of molten Ag by the time of 2.5 ns, as can be seen from the series of snapshots shown in Fig. 4.

The distinctly different dynamics at the plume–water interface observed in the simulations performed with laser pulse durations of 10 and 400 ps can be understood by considering the characteristic times of redistribution of the deposited laser energy by the thermal conduction and stress waves, τ_{th} and τ_{s}, respectively. By relating τ_{th} and τ_{s} to the time of the laser-induced heating, which can be taken as the laser pulse duration, τ_{p}, or the characteristic time of the electron–phonon equilibration,

$\tau_{\text{e–ph}}$, whichever is longer, the conditions of thermal and stress confinement can be formulated.[28,30,33,34,57] The condition of thermal confinement, in particular, can be expressed as $\max\{\tau_{\text{p}}, \tau_{\text{e–ph}}\} \leq L_{\text{c}}^2/(2D_{\text{T}})$, where $\max\{\ldots\}$ denotes the selection of the largest of the two time constants, L_{c} is the diffusive/ballistic penetration depth of the excited electrons before the electron–electron and the electron–phonon equilibration, and D_{T} is the thermal diffusivity of the target material. The condition of stress confinement can be expressed as $\max\{\tau_{\text{p}}, \tau_{\text{e–ph}}\} \leq L_{\text{c}}/C_{\text{s}}$, where C_{s} is the speed of sound in the target material.

Using the estimates provided in ref. 57 for the ultrashort pulse laser interaction with Ag, namely, $\tau_{\text{e–ph}} \approx 8$ ps, $L_{\text{c}} \approx 140$ nm, $D_{\text{T}} = 1.47 \times 10^{-4}$ m^2 s^{-1} (near melting temperature), and $C_{\text{s}} = 3650$ m s^{-1}, we conclude that the conditions of both thermal and stress confinement are satisfied for $\tau_{\text{p}} = 10$ ps, and neither thermal nor stress confinement is realized for $\tau_{\text{p}} = 400$ ps. The absence of the stress confinement in the case of 400 ps laser pulse means that the region heated by the laser can undergo mechanical relaxation (expansion) during the laser pulse. As a result, the maximum compressive pressure observed in this simulation reduces down to ~ 4.8 GPa with respect to almost 8 times higher maximum pressure of 38 GPa recorded in the simulation performed with 10 ps laser pulse. The absence of the thermal confinement for the 400 ps pulse irradiation allows for a substantial heat diffusion away from the region of the initial electron–phonon thermalization of the deposited laser energy, which is manifested by a reduction of the maximum temperature from $\sim 12\,000$ to ~ 8000 K as the laser pulse duration increases from 10 to 400 ps.

The effective thermal conduction to the bulk of the target and the reduced level of mechanical stresses result in a "gentler" ablation observed in the simulation performed with 400 ps laser pulse. The much lower mechanical stresses, in particular, limit the depth from which the initial material ejection occurs to the depth where the temperature exceeds the threshold level required for the onset of the phase explosion, ~ 186 nm. In contrast, at the same laser fluence, the dynamic relaxation of strong laser-induced stresses generated upon irradiation by 10 ps laser pulse leads to the ejection of additional colder parts of the molten material, down to ~ 325 nm below the initial surface.[8] Moreover, for 10 ps laser pulse, the collision of the colder material ejected from deeper regions of the target with the hot metal layer formed at the plume–water interface is found to be responsible for jetting of the melt into the cold/dense water environment, beyond the boundary of the cavitation bubble.[8,41] For 400 ps laser pulse, without the ejection of colder droplets driven by the relaxation of photomechanical stresses, no jetting from the plume–water interface is observed.

As can be seen from Fig. 3, the interaction of the ablation plume with water environment can be separated into two stages. At the first stage, the top part of the irradiated target undergoes phase explosion, rapidly expands, and pushes the overlying water away from the target. The resistance of the water environment decelerates the ablation plume and, by the time of ~ 2 ns, stops the outward motion of the plume accumulated near the interface with water. A big fraction of the ablation plume is then reflected back and is eventually redeposited on the target.
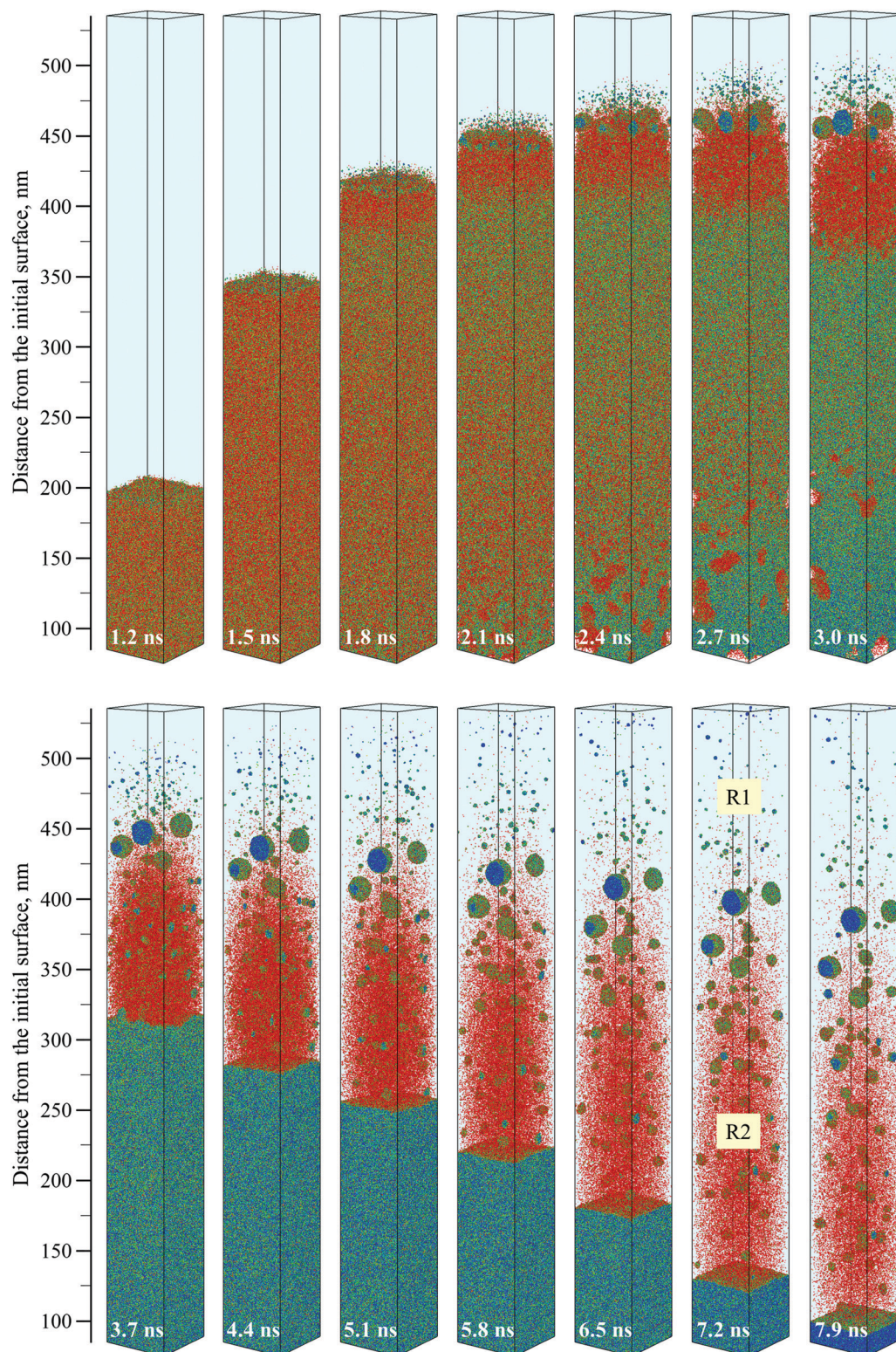
Fig. 4 Snapshots of atomic configurations predicted in a large-scale atomistic simulation of a bulk Ag target irradiated in water by a 400 ps laser pulse at an absorbed fluence of 600 mJ cm^{-2}. Only a part of the computational system from 85 to 535 nm with respect to the initial surface of the Ag target is shown in the snapshots. The atoms are colored according to their potential energies, from blue for molten Ag to red for vapor-phase Ag atoms. The molecules representing water environment are not shown (see Fig. 5 for clarification), and the presence of water is illustrated schematically by a light blue background color. Animated sequence of snapshots from this simulation with a time resolution of 100 ps is provided as ESI,† for this article.

7084 | *Phys. Chem. Chem. Phys.*, 2020, **22**, 7077−7099

This journal is © the Owner Societies 2020
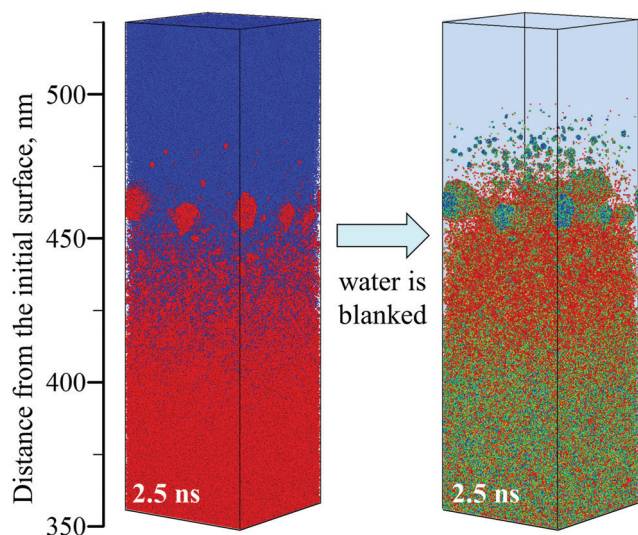
Fig. 5 An illustration of the approach adopted for plotting snapshots of atomic configurations. The coarse-grained particles representing water environment are shown in the left snapshot and are deleted (blanked) in the right one, with both images showing the same part of the computational system at 2.5 ns after the start of the simulation illustrated in Fig. 3 and 4. The latter representation provides a clear view of the processes responsible for nanoparticle generation and is used in Fig. 4 and 6. In the left image, the water molecules and Ag atoms are shown by blue and red colors, respectively. In the right image, the atoms are colored according to their potential energies, from blue for molten Ag to red for vapor-phase Ag atoms.

This stage proceeds in a manner similar to that observed in the simulation performed with a shorter 10 ps laser pulse,[8] although in the case of the shorter pulse a more vigorous expansion assisted by the relaxation of laser-induced stresses results in the formation of a much denser layer that is pushed further away from the target prior to the reflection and redeposition. The maximum heights reached by the fronts of the ablation plume by the end of the plume deceleration stage, ∼2 ns, are 550 and 460 nm above the initial surface in the simulations performed with 10 and 400 ps laser pulses, respectively.

Following the first dynamic stage of the plume interaction with water environment, the second much slower stage starts, where the upper part of the hot metal plume mixes with water, leading to the formation and expansion of a low-density mixing region. The water in contact with the hot metal is heated up to the supercritical state, and the expansion of the supercritical water mixed with metal vapor drives the expansion of the low-density region. The extent of metal–water mixing is shown by two black lines in Fig. 3a and b, which mark the maximum and minimum heights where both Ag atoms and water molecules are present. The appearance and expansion of the low-density mixing region can be seen more clearly from the density profiles shown in Fig. 3c. A region where the densities of both metal and water are more than twice lower than the corresponding densities of the adjacent metal layer and compressed water environment can already be seen in the profiles shown at 2 ns. This region undergoes rapid expansion during the following several nanoseconds, reaching the width of ∼170 nm

by 3.5 ns (Fig. 3b and c) and ∼450 nm by 8 ns (Fig. 3b). While it would be misleading to directly map the values of density of nonequilibrium mixture of vapor, clusters, and small droplets to the equilibrium phase diagram calculated for the model Ag material and provided in the Appendix (see Fig. 13a), we note that the density of Ag in the mixing region is already below the critical density of 2.29 g cm^{-3} at 2 ns (Fig. 3c), suggesting that the material in this region is partially vaporized. Further expansion of the mixing region leads to the additional reduction of the density of Ag down to the levels characteristic of the vapor phase, with bumps on the density profile reflecting the presence of nanoparticles. A visual analysis of the simulation snapshots (Fig. 4) supports these conjectures.

Up to ∼7 ns, the expansion of the mixing region proceeds more actively in the direction towards the target, where the motion of the hot metal layer pushed back by the water environment meets almost no resistance as it moves through the gap between the remaining target and the hot metal layer, Fig. 3b. This gap is filled with a low-density metal vapor that remains rarified despite the compression caused by the shrinkage of the gap. The sustained low density of the metal vapor in this region during the compression (∼0.014 g cm^{-3} at 5 to 7 ns) can be explained by the condensation to the target surface, which is cooled down to ∼1100 K by 7 ns due to the heat transfer to the bulk of the target, Fig. 3a. The gap between the hot metal layer and the target surface closes, and the downward expansion of the low-density region ends at ∼7 ns, when the layer is redeposited to the target. As soon as the redeposited layer comes into contact with the colder target, it rapidly cools down and densifies, Fig. 3a and b.

The upward expansion of the low-density region is expected to continue on a timescale much longer than those accessible in atomistic simulations, producing a cavitation bubble commonly observed in PLAL experiments.[2–11,19–23] The expansion rate observed at 5–8 ns, if sustained, would bring the boundary of the cavitation bubble to 5 μm by the time of 1 μs, while the abrupt end of the downward expansion of the low-density region upon the redeposition of the metal layer at ∼7 ns can be expected to further facilitate the upward expansion. This rough estimation of the rate of the cavitation bubble expansion is at the lower end of those observed in the experiments,[7,8] although a direct continuum-level multi-phase modeling of the long-term cavitation bubble dynamics[65,66] is needed for establishing quantitative connections to the results of experimental probing of the cavitation bubble dynamics.

In the discussion provided above, the low-density metal–water mixing region is treated as a single entity. A mere visual analysis of the density contour plot in Fig. 3b and the snapshots of atomic configurations shown in Fig. 4 reveal that the mixing region consists of two distinct sub-regions separated by a group of large nanoparticles. These sub-regions are marked as R1 and R2 in the density plots in Fig. 3 and the snapshot shown for a time of 7.2 ns in Fig. 4. The atoms in the snapshots are colored by their potential energies, with vapor-phase Ag atoms having the highest potential energy and colored red. The abundance of the vapor-phase atoms in sub-region R2 and a much lower

This journal is © the Owner Societies 2020

Phys. Chem. Chem. Phys., 2020, 22, 7077–7099 | 7085
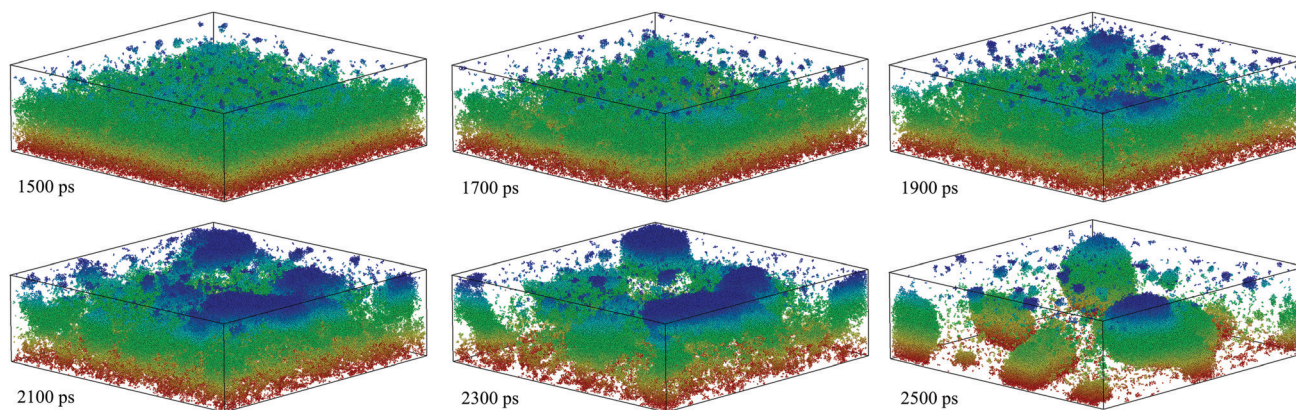
Fig. 6 Enlarged views of a 15 nm-thick layer formed at the interface between the ablation plume and water environment in the simulation illustrated by snapshots in Fig. 4. The location of this dense transient layer is marked by the dashed line in Fig. 3a and b. Water molecules are not shown, and the coloring is based on the vertical coordinate of atoms ranging from red to blue in each snapshot. The snapshots illustrate the plume accumulation, deceleration, and cooling due to the interaction with water environment, leading to the formation of large liquid droplets.

density of such atoms in sub-region R1 are apparent from the snapshots. Moreover, the nanoparticles generated in sub-region R2 are much larger than those formed in sub-region R1. A detailed discussion of the distinct mechanisms and kinetics of the nano-particle generation in the two regions is provided below, in Section 3.2. At the end of this section, we only briefly describe the processes leading to the appearance of the two distinct sub-regions separated by a narrow interfacial layer that promptly decomposes into a group of large (>10 nm) nanoparticles.

As discussed above, the initial interaction of the ablation plume with water environment leads to the rapid deceleration of the plume and accumulation of the ejected material at the plume–water interface. As can be seen from the density profiles shown for 1.4 ns in Fig. 3c and the snapshots shown for 1.2 and 1.5 ns in Fig. 4, the plume–water interface remains relatively sharp at the initial stage of the rapid ablation plume expansion. Rapid deceleration of the plume and cooling of the metal in direct contact with the water environment, however, causes roughening of the interfacial layer and its decomposition into several large nanoparticles with diameters on the order of 10 nm by ∼2.5 ns. To better illustrate the process of the interfacial layer decomposition, several enlarged views of a 15 nm-thick interfacial layer are shown in Fig. 6. The rapid decomposition of the interfacial layer can be attributed to the fast cooling and condensation in the top part of the plume due to the interaction with water environment, combined with the development of Rayleigh–Taylor instability at the interface between the heavier metal layer decelerated by lighter water environment, similar to that discussed for shorter pulses in ref. 8, 40 and 41. The location of the interfacial layer that undergoes the decomposition into large nanoparticles can be identified from pronounced peaks at the front of the Ag density profiles in Fig. 3c. The location of the layer and the subsequent averaged positions of three largest nanoparticles that originate from this layer are marked by the black dashed lines in Fig. 3a and b.

The decomposition of the interfacial layer lets the super-critical water stream downward and interact with the part of the

ablation plume retreating towards the target. This interaction triggers a rapid formation of relatively large nanoparticles due to spinodal decomposition of the expanding Ag rapidly cooled from the supercritical state (note that the critical temperature of the model EAM Ag is T_c = 3360 K, as identified in the calculations described in the Appendix). As the lower part of the hot metal layer moves towards the target, it is joined with the colder material ejected from deeper parts of the target, leading to cooling and densification of the layer (Fig. 3a and b), with a simultaneous sharpening of the interface between the metal layer and the R2 part of the low-density mixing region (*cf.* density profiles for Ag at 2.5, 3, and 3.5 ns in Fig. 3c).

Both water and metal atoms are present not only below but also above the interfacial region, *i.e.*, in sub-region R1. In this sub-region, the density of the metal is much lower, the density of water is higher, and the temperature is lower, as compared to sub-region R2. The origin of the metal atoms, clusters and nanoparticles in sub-region R1 is also different from that in sub-region R2. The main source of metal atoms in sub-region R1 is the active evaporation from the hot plume–water interface formed during the initial plume expansion. The evaporation subsides by the time the interfacial region cools down due to the interaction with water and decomposes into the large nanoparticles, *i.e.*, by ∼2.5 ns. The hot metal vapor in sub-region R1 mixes with supercritical water, rapidly cools down, and condenses into clusters and nanoparticles, as discussed and quantified in the next section.

3.2. Nanoparticle generation mechanisms and evolution of their size distribution

Based on the discussion of processes occurring during the short pulse PLAL provided in the previous section, three distinct nanoparticle generation mechanisms operating at different stages of the ablation process and in different parts of the ablation plume can be identified. These three mechanisms, leading to the generation of three groups of nanoparticles with distinctive characteristic sizes, are discussed next.

7086 | *Phys. Chem. Chem. Phys.*, 2020, **22**, 7077–7099

This journal is © the Owner Societies 2020

First, the formation of a thin transient metal layer at the interface between the ablation plume and water environment followed by its subsequent decomposition is responsible for the generation of large nanoparticles at the early stage of the ablation process. This process is illustrated in Fig. 6, where the emergence of three nanoparticles with final diameters of 16.5 nm (134 239 atoms), 14.3 nm (87 593 atoms), and 12.5 nm (59 382 atoms) can be observed by the time of 2.5 ns. Note that, because of the use of periodic boundary conditions, some of the nanoparticles may be "split" by the boundaries and different parts of the same nanoparticle may appear on opposite sides of the computational cell in the snapshots shown in Fig. 4–6. As discussed in the previous section, the roughening and decomposition of the interfacial layer are caused by the fast cooling and deceleration of the top part of the plume that comes into direct contact with the water environment. While these processes are similar to those responsible for the roughening of the plume–water interface observed in simulations of PLAL performed with ultrashort laser pulses,[8,40,41] the lower density of the metal layer accumulated near the plume–water interface enables more extensive mixing with water and facilitates the decomposition of the top part of the metal layer into individual nanoparticles. The products of the layer decomposition remain inside the emerging cavitation bubble and are not ejected beyond the boundary of the bubble, as has been observed in modeling and experimental probing of ultrashort laser ablation of bulk Ag and Au targets.[8,19,41] We note that recent MD simulations of ultrashort PLAL under conditions of spatially modulated laser energy deposition[42] suggest that prompt disintegration of the interfacial layer into nanoparticles can be caused by lateral pressure gradients, leading to the elimination of the largest nanoparticles that may form in the course of slower layer decomposition.

The thermal history of the material that ends up in the three large nanoparticles, shown in Fig. 7, reflects the processes
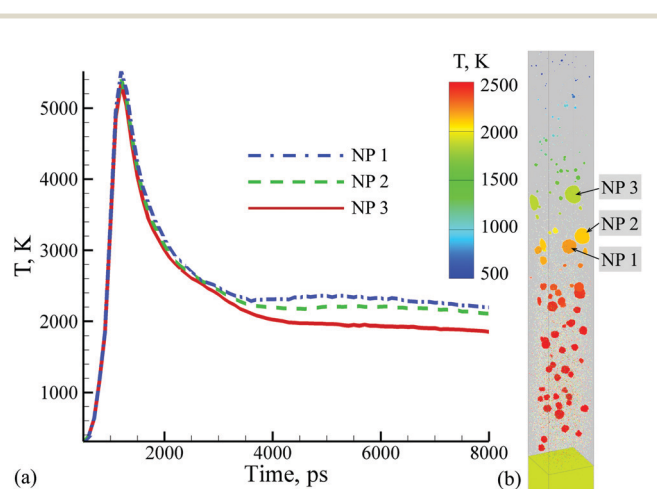
responsible for their formation. During the laser pulse, the material is superheated significantly above the critical temperature. Rapid expansion of the ablation plume and its interaction with water leads to the temperature drop by about a factor of two within the following nanosecond. This temperature drop coincides with decomposition of the interfacial metal layer into large nanoparticles. Further cooling of the nanoparticles located in the middle of the low-density metal–water mixing region becomes much slower, and the temperature of the nanoparticles is still above 1850 K, $i.e.$, more than 60% above the equilibrium melting temperature of the model EAM Ag, $T_m = 1139$ K, at the end of the simulation, 8 ns. This slow cooling can be contrasted with the rapid quenching and freezing of some of the large (10s of nm) nanoparticles observed in the simulations performed with ultra-short laser pulses,[8,41] where the large nanoparticles generated by a cascade of hydrodynamic instabilities and injected into dense water environment are rapidly quenched by the surrounding water and crystallize within several nanoseconds.

The second distinct group of nanoparticles can be identified in the upper part of the low-density mixing region, above the transient interfacial layer and large nanoparticles marked by the black dashed lines in Fig. 3, $i.e.$, in sub-region R1 defined in the previous section. The small nanoparticles in this region appear at the early stage of the plume expansion and can already be seen near the front of the expanding plume starting from around 1 ns, when the dense transient layer is just starting to form and detach from the plume front. In particular, a large number of nanoparticles can be seen at 1.5 ns in the enlarged snapshot of the plume–water interface shown in Fig. 6, and the nanoparticles are clearly visible throughout the expanding sub-region R1 in Fig. 4 at later times.

The kinetics of the nanoparticle formation in sub-region R1 is illustrated by Fig. 8a, where the time evolution of the cumulative number of atoms present in this region in the form of vapor (individual atoms), small clusters consisting of less than 30 atoms (effective diameters below 1 nm), and nanoparticles of different sizes is plotted, as well as by Fig. 9, where the nanoparticle size distributions are shown for different times. From Fig. 8a, we see that at early times, before 2 ns, the Ag atoms appear in this region in the form of vapor-phase atoms and small clusters, reflecting the fact that the Ag atoms are emitted into this sub-region from the hot transient metal layer generated at the plume–water interface during the initial stage of the ablation plume expansion. The interface is rapidly cooled from the supercritical state down to below T_c by ~2 ns and to below $0.7 T_c$ by 3 ns, as can be seen from the temperature profiles plotted in Fig. 7a for the interfacial material contributing to the large nanoparticles. The rapid cooling shuts down the active evaporation from the interfacial metal layer, leading to the saturation of the total number of Ag atoms in sub-region R1 after 2 ns. The transient drop in the total number of atoms in this region between 2.5 and 3.5 ns, followed by a recovery during the next nanosecond, can be explained by the exchange in the vapor-phase atoms between sub-regions R1 and R2. The decomposition of the dense interfacial layer into nanoparticles enables an outflow of the Ag atoms from the higher-pressure

Fig. 7 The time dependence of the temperatures of groups of atoms that end up in the three large nanoparticles produced through the disintegration of the transient dense metal layer formed at the plume−liquid interface (a), and a snapshot of the final configuration taken at a time of 8 ns, with atoms colored by the local temperature (b).

This journal is © the Owner Societies 2020

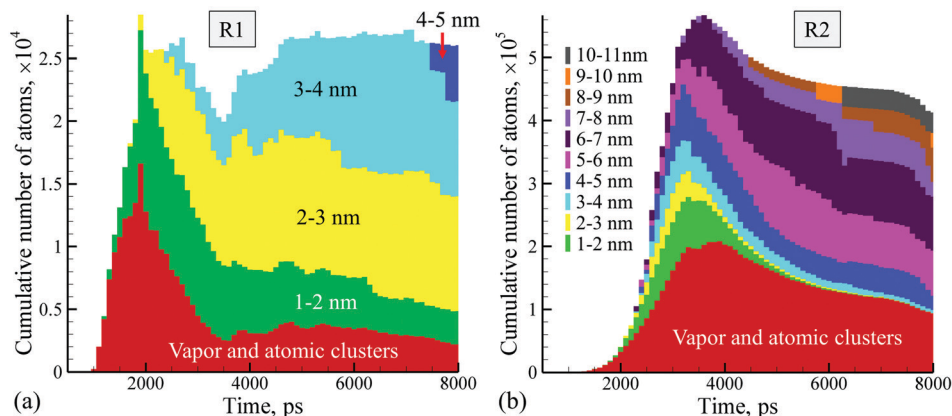$Phys. Chem. Chem. Phys.$, 2020, **22**, 7077–7099 | **7087**

Fig. 8 Results of the analysis of nanoparticles generated in a simulation illustrated by Fig. 3–7: the cumulative numbers of atoms that belong to the vapor phase and atomic clusters with diameters less than 1 nm (red color), and nanoparticles of different sizes (color coding by nanoparticle diameters, as defined in the legend) identified at different times during the simulation in sub-regions (a) R1 and (b) R2 defined in Fig. 3. Large nanoparticles produced as a result of decomposition of a transient interfacial layer illustrated in Fig. 6 are not included in the analysis illustrated by this figure.
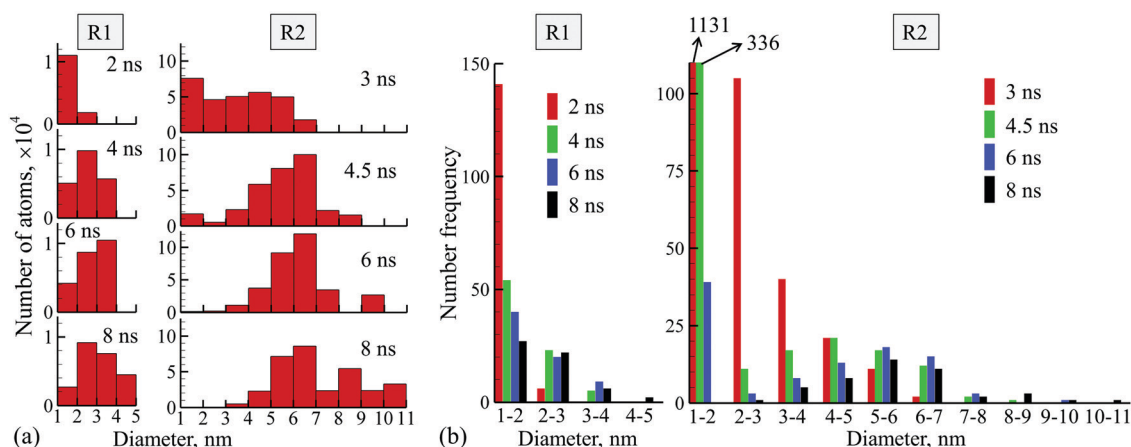

Fig. 9 Results of the analysis of nanoparticles generated in a simulation illustrated by Fig. 3–7: nanoparticle size distributions shown for different times during the simulation in the form of (a) the number of atoms in nanoparticles of different sizes (above 1 nm) and (b) number frequency of the nanoparticles. The distributions are calculated separately for sub-regions R1 and R2 defined in Fig. 3. Large nanoparticles produced as a result of decomposition of a transient interfacial layer illustrated in Fig. 6 are not included in the distributions.

sub-region R1 to the underlying subregion R2. At a later time, the much higher density of Ag atoms in sub-region R2, combined with the downward motion of the large clusters defining the boundary between the two sub-regions, results in the redistribution of the Ag atoms in the opposite direction, from sub-region R2 to sub-region R1.

While the total number of Ag atoms in sub-region R1 stays roughly constant after 2 ns, there is a clear redistribution of the atoms from vapor and small atomic clusters to nanoparticles with increasingly larger sizes, reaching the range of 4–5 nm by 7.5 ns. This observation reflects the process of rapid nucleation and growth of nanoparticles from Ag vapor cooled by the interaction with surrounding supercritical water. The steady growth of the nanoparticles is also reflected in the evolution of the nanoparticle size distribution shown for sub-region R1 in Fig. 9, where the number of small nanoparticles with diameters in the range of 1–2 nm is decreasing with time, while

the increasingly large nanoparticles appear in the distribution as time progresses.

The generation of nanoparticles through the rapid nucleation and growth in the low-density metal–water mixing region is the mechanism that has also been identified in the simulations of ultrashort pulse laser ablation of Ag in water.[8,40,41] It is particularly instructive to compare the results discussed above to those obtained in a simulation reported in ref. 8, where the same absorbed laser fluence of 600 mJ cm^{-2} and the same lateral size of the computational cell are used, and the only difference is that the target is irradiated by a shorter 10 ps laser pulse. The evolution of both the cumulative number of atoms and nanoparticle size distribution, provided in the ESI for ref. 8, are qualitatively similar to those shown for sub-region R1 in Fig. 8 and 9. One difference is that, contrary to the saturation of the cumulative number of atoms after 2 ns observed in Fig. 8a, the number of atoms in the metal–water mixing region generated in ultrashort PLAL exhibits

a steady increase during the whole duration of the simulation reported in ref. 8, *i.e.*, 5.5 ns. This continuous increase in the number of Ag atoms can be attributed to the fact that the low-density mixing region stays in the immediate contact with the dense and hot metal layer that serves as a source of metal vapor. In contrast, in the simulation performed with longer 400 ps laser pulse, the dense metal layer is separated from sub-region R1 by a low-density sub-region R2, which prevents the direct supply of Ag vapor from the dense and hot metal layer to sub-region R1.

As a result of the continuous increase in the number of atoms in the low-density mixing region in the simulation performed with 10 ps laser pulse, the total number of atoms reached in this region by 5.5 ns is about twice larger than that in the simulation performed with 400 ps laser pulse. The overall picture of the nanoparticle nucleation and growth, reflected in the gradual redistribution of atoms from vapor and small clusters to nanoparticles with increasing diameter, however, is similar in both simulations. Moreover, the maximum size of the nanoparticles generated through this mechanism by 5.5 ns in the simulation reported in ref. 8 is the same as that produced by 8 ns in the simulation reported in this paper, 4–5 nm in diameter, as can be seen from Fig. 8a and 9. The observation of the formation of nanoparticles through the nucleation and growth in the low-density metal–water mixing region in simulations of PLAL performed for bulk Ag targets irradiated by 100 fs,[41] 10 ps,[8] and 400 ps laser pulses, as well as for thin Ag films irradiated by 40 fs laser pulses,[40] suggests that this mechanism is a common route of the nanoparticle generation in PLAL, regardless the pulse duration and target geometry.

Finally, the third and the most numerous group of nanoparticles emerges in sub-region R2 after a time of 2 ns, as can be seen from Fig. 4, 8b and 9. As discussed in the previous section, the formation of nanoparticles in this sub-region can be attributed to the spinodal decomposition of the top part of the ablation plume undergoing simultaneous expansion due to the reflection of the ablation plume from the water environment and mixing with the supercritical water. From Fig. 8b, we can see that the spinodal decomposition results in almost simultaneous formation of nanoparticles with a broad range of diameters, up to 7 nm, within a relatively short time span between 2 and 3 ns. The mass-weighted size distribution of nanoparticles generated in sub-region R2 by 3 ns is relatively flat, Fig. 9a, but undergoes a marked shift to the right, in the direction of larger nanoparticles, as time progresses. Notably, the number of Ag atoms in smaller nanoparticles with sizes less than 4 nm rapidly drops, as can also be seen from Fig. 8b, where the fields corresponding to nanoparticles with diameters from 1 to 4 nm visually collapse to almost a single line by the end of the simulation. Most dramatically, the disappearance of small nanoparticles can be seen from the size distributions provided in the form of number frequency of nanoparticles of different sizes, Fig. 9b, where we see that the number of nanoparticles in the range from 1 to 2 nm drops from 1131 at 3 ns, to 336 at 4.5 ns, to 39 at 6 ns, and to zero at 8 ns. Similarly, the number of nanoparticles in the range from 2 to 3 nm drops from 105 to 1 during the same time period.

The sharp drop in the number of small nanoparticles and complete disappearance of the smallest nanoparticles are incompatible with the nucleation and growth mechanism discussed above for sub-region R1. Indeed, the nucleation of new nanoparticles from vapor or growth of the atomic clusters would continuously generate nanoparticles with small diameters. The complete disappearance of such nanoparticles suggests that this route of the nanoparticle generation is blocked by thermodynamic conditions in sub-region R2, while the appearance of increasingly large nanoparticles can be attributed to the collision and coalescence of smaller nanoparticles as well as the growth of the largest nanoparticles through condensation of the vapor-phase atoms.

To explain the difference between the processes responsible for the nanoparticle formation in sub-regions R1 and R2, we use the thermodynamic properties of the model EAM Ag to evaluate the thermodynamic conditions leading to the size-dependent condensation or evaporation of the nanoparticles (liquid droplets). First, the critical diameter required for the nanoparticle condensation, D_{cr}, is evaluated as a function of vapor number density, n, and temperature, T, using the Gibbs–Kelvin equation that relates the curvature of the liquid–vapor interface to the saturation vapor pressure.[67] Assuming the proportionality between the vapor pressure and density, D_{cr} of a droplet at equilibrium with vapor of density n can be expressed as

$$D_{cr} = 4\sigma/[n_l k_B T \ln(n/n_v)], \quad (1)$$

where σ is the surface tension of the liquid–vapor interface, n_l, and n_v are the equilibrium number densities of liquid- and vapor-phase Ag (separated by a flat interface), respectively. The values of σ, n_l and n_v are calculated at different temperatures and fitted to obtain continuous temperature dependencies as described in the Appendix. The field of $D_{cr}(n, T)$ is then calculated with eqn (1), shown in the form of a contour plot in Fig. 10, and used as a background for plotting the thermodynamic conditions realized at different times in sub-regions R1 and R2. These thermodynamic conditions are obtained by averaging over the sub-regions R1 and R2 (the large nanoparticles produced at the boundary between the sub-regions through disintegration of the interfacial layer are not included in the averaging) and are provided in Table 1. While our intention is to show the parameters of the vapor phase in the two sub-regions, the low number of monomers in sub-region R1 (from 38 at 3 ns down to 20 at 8 ns) makes the reliable evaluation of temperature difficult. Therefore, the temperature values for the data points plotted in Fig. 10 are the result of averaging over atoms and clusters consisting of less than 30 atoms (effective diameter below 1 nm).

The locations of the circles and triangles with respect to the field of $D_{cr}(n, T)$ in Fig. 10 clearly illustrate the difference in the thermodynamic conditions related to the nanoparticle growth realized in these two regions during the first nanoseconds of the ablation process. In the sub-region R1, the Ag atoms evaporated from the interfacial layer are rapidly cooled by the surrounding supercritical water and condense into clusters and nanoparticles through the barrierless nucleation and growth process.

This journal is © the Owner Societies 2020

Phys. Chem. Chem. Phys., 2020, **22**, 7077–7099 | **7089**
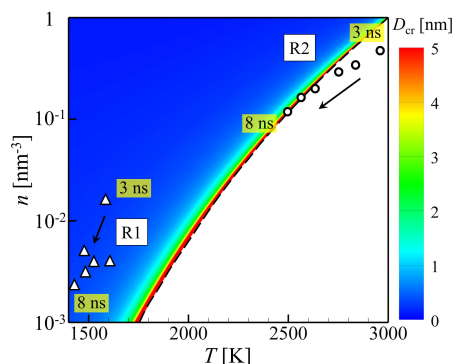
Fig. 10 The contour plot outlining the critical (minimum) diameter of particles that can grow by condensation from the surrounding vapor under specific temperature T and Ag vapor density n conditions calculated based on the Gibbs−Kelvin equation. The dashed line shows the saturation condition for a flat vapor−liquid interface. The blue part of the field corresponds to conditions where all nanoparticles can grow by condensation, while the white area corresponds to conditions where particles of any size should evaporate. The conditions realized in sub-regions R1 and R2, summarized in Table 1, are shown by triangles (n_{R1}, T_{R1}^{1nm}) and circles (n_{R2}, T_{R2}^{1nm}), respectively.

Table 1 Thermodynamic parameters averaged over sub-regions R1 and R2 defined in Fig. 3: number density of Ag monomers (n), temperature averaged over Ag monomers and clusters with effective diameters below 1 nm (T^{1nm}), and temperature averaged over all Ag atoms (T^{all}). The subscripts R1 and R2 denote the sub-region for which the calculations are performed. The large nanoparticles produced at the boundary between the two sub-regions through disintegration of the interfacial layer are not included in the calculation of T_{R1}^{all} and T_{R2}^{all} (the temperature evolution of these nanoparticles is shown in Fig. 7a)

	Sub-region R1			Sub-region R2		
Time [ps]	n_{R1} [nm^{-3}]	T_{R1}^{1nm} [K]	T_{R1}^{all} [K]	n_{R2} [nm^{-3}]	T_{R2}^{1nm} [K]	T_{R2}^{all} [K]
3000	1.5×10^{-2}	1592	1453	0.49	2988	3066
4000	5.3×10^{-3}	1478	1224	0.35	2839	2818
5000	4.0×10^{-3}	1613	1277	0.28	2729	2744
6000	4.0×10^{-3}	1523	1292	0.20	2621	2608
7000	3.2×10^{-3}	1484	1306	0.16	2572	2539
8000	2.4×10^{-3}	1433	1237	0.12	2495	2467

Indeed, all the triangles are located deep into the blue part of the D_{cr} (n, T) contour plot, where the critical diameter for nanoparticle condensation is comparable to interatomic distance in the liquid state. While the physical model behind eqn (1) becomes invalid for such small diameters, the thermodynamic conditions leading to the vanishing critical diameter are still indicative of the barrierless nucleation. The process of barrierless nucleation and growth is reflected in the sequential redistribution of Ag atoms from vapor and small atomic clusters to nanoparticles in Fig. 8a as well as in the evolution of the nanoparticle size distributions shown for sub-region R1 in Fig. 9 and discussed above.

In contrast to sub-region R1, the points for sub-region R2 (circles in Fig. 10) are initially located within the white part of the contour plot, which corresponds to conditions of undersaturation, where nanoparticles of all sizes should evaporate rather than grow. As time progresses, the points approach and

enter (at 7 and 8 ns) the region where the largest nanoparticles are above the critical radius for growth. This observation explains the rapid disappearance of small nanoparticles in sub-region R2, which is apparent from Fig. 8b and 9. According to the calculation of the average vapor density and temperature, however, all nanoparticles should shrink/evaporate, which contradicts the observation of a steady rise in the population of large nanoparticles. The increase in the number of large nanoparticles can be explained by two factors. First, the high density of the ablation plume in sub-region R2 facilitates the formation of larger nanoparticles through the collision and coalescence of smaller ones. Second, the nonuniformity of the temperature distribution within sub-region R2 may also play a role. The temperature nonuniformity can be seen from the snapshot shown in Fig. 7b, where the atoms are colored by local temperature. The upper part of sub-region R2, where the largest nanoparticles are located, is somewhat colder, and the conditions for growth of large nanoparticles by vapor condensation may be realized there at earlier times.

The comparison of temperature values averaged over all atoms, T^{all}, and small atomic clusters, T^{1nm}, in sub-regions R1 and R2, listed in Table 1, also reflects the difference in the processes of the nanoparticle formation in the two sub-regions. In sub-region R1, the vapor phase atoms and small atomic clusters have temperature that is consistently higher than the temperature calculated by averaging over all atoms in this sub-region, i.e., $T_{R1}^{1nm} > T_{R1}^{all}$. This observation reflects the sequential redistribution of atoms from vapor to clusters and to nanoparticles in the barrierless nucleation and growth occurring in this sub-region and discussed above. The vapor has relatively high initial temperature, since it originates from the hot interfacial metal layer as well as the large nanoparticles generated from the decomposition of this layer. As the vapor condenses into clusters and nanoparticles, the temperature drops due to the interaction with water environment. The larger is a nanoparticle, the longer it has been present in the dense water environment and has experienced cooling by the water. In contrast, the rapid decomposition of the hot metal expanding from the supercritical state in sub-region R2 produces a dense mixture of vapor and nanoparticles that undergoes a rapid thermal equilibration between the different plume components. The nanoparticles emerge from the decomposition with somewhat higher temperatures,[31,32] as reflected by $T_{R2}^{all} > T_{R2}^{1nm}$ at 3 ns, but the difference between T_{R2}^{all} and T_{R2}^{1nm} becomes statistically insignificant at later times.

The location-dependent cooling of nanoparticles within the expanding low-density metal–water mixing region at the initial stage of the cavitation bubble expansion has important implications for the long-term evolution of the nanoparticle size distribution. The small nanoparticles formed in sub-region R1 through the nucleation and growth at the front of the mixing region are already cooled down by the surrounding dense water environment to temperatures below the melting temperature (blue color in Fig. 7b) and crystallize by the end of the simulation. Similarly fast cooling and freezing of nanoparticles at the front of the expanding cavitation bubble have

7090 | Phys. Chem. Chem. Phys., 2020, 22, 7077–7099

This journal is © the Owner Societies 2020

been predicted in simulations performed with ultrashort laser pulses[8,40,41] and observed in recent time- and spatially-resolved X-ray probing of nanoparticles present in different parts of the cavitation bubble generated by 12 ps pulse laser ablation of Au and Ag.[19]

In contrast to the rapid quenching of the small nanoparticles at the front of the emerging cavitation bubble, the large nanoparticles generated by disintegration of the interfacial region undergo much slower cooling following their formation at ~ 2.5 ns and still have temperatures above $1.6 T_m$ at the end of the simulation (Fig. 7a). The temperature of nanoparticles generated below the interfacial layer, in sub-region R2, is even higher, with the average temperature of $T_{R2}^{all} = 2467$ K $= 0.73 T_c = 2.17 T_m$ calculated for this sub-region at the end of the simulation (Table 1). Given the relatively low rate of cooling and the high density of the molten nanoparticles in the lower part of the cavitation bubble (interfacial region and underlying sub-region R2), it is reasonable to expect that the process of collision and coalescence of the nanoparticles will play a major role in defining the long-term evolution of the nanoparticle size distribution. Moreover, the formation of nanoparticles through liquid-phase coalescence and relatively slow cooling can be expected to yield spherical crystalline nanoparticles featuring close-to-equilibrium microstructure. Note that, while the addition of salts or other surfactants to the liquid environment has been demonstrated to be effective in quenching the nanoparticle size distribution,[21,22,68–70] the ability of surfactants to prevent or reduce the coalescence of molten nanoparticles at this early stage of the ablation process is questionable due to the low density and high temperature of the supercritical water in this region, as well as the complexity of its interaction with the nanoparticles. The results of recent time-resolved experimental probing of the nanoparticle formation,[21] though, reveal that the nanoparticle size quenching by salts added to the liquid environment can already be observed by 90 μs after the laser pulse, *i.e.*, at a time when the cavitation bubble is still expanding. These results indicate that the nanoparticle-ion interactions responsible for the size reduction may indeed occur in the low-density environment of the cavitation bubble.

The observation that the total number of atoms in sub-region R2 is about 20 times larger than that in sub-region R1 (Fig. 8) suggests that the total yield of the nanoparticles can be larger for the same amount of the deposited laser energy (*i.e.*, the same absorbed fluence) when the target is irradiated by a short (hundreds of picoseconds or nanoseconds) rather than ultrashort (tens of picoseconds or shorter) laser pulses, as the sub-region R2 does not appear in the latter case. Moreover, the population of nanoparticles produced by the three mechanisms discussed above is likely to have a broad size distribution, with nanoparticles generated in sub-region R2 filling the intermediate range between the smallest ones quenched at the front of the cavitation bubble and the large ones formed by the interfacial layer decomposition. While the prediction of the higher nanoparticle yield produced by the short laser pulses still awaits confirmation by experiments where the absorbed energy is carefully controlled and characterized, the broad size distributions are, indeed, commonly observed in experiments performed with short laser pulses.[21,25,49–51] In contrast, nanoparticles produced with ultrashort laser pulses, where sub-region R2 does not appear,[8] can exhibit pronounced bimodal size distributions[8,45–48] reflecting the presence of two distinct groups of nanoparticles generated through two different mechanisms.[8,40–42]

The spatial distribution of nanoparticles within the expanding cavitation bubble, predicted in the simulations, can be related to the results of time-resolved SAXS experiments probing the process of nanoparticle generation within the cavitation bubble. In particular, the experimental observation that large nanoparticles can be detected at the early stage of the bubble expansion and tend to be concentrated in the upper part of the bubble[19–21] is consistent with the mechanism of the large nanoparticle formation through the decomposition of a hot metal layer generated at the plume–water interface predicted in the simulations.

3.3. Laser ablation in liquid: nanosecond pulses

As demonstrated in the previous section, the increase of the pulse duration from 10 ps to 400 ps leads to significant changes in the dynamics of the ablation process and nanoparticle generation mechanisms. As discussed in Section 3.1, the pulse duration of 400 ps is sufficiently long to ensure the absence of thermal and stress confinement characteristic of ultrashort pulse laser ablation. It is reasonable to expect that further increase of the pulse duration to nanoseconds, commonly used in PLAL experiments, would not lead to qualitative changes in the nanoparticle formation mechanisms. The direct verification of this expectation in atomistic simulations, however, is challenging for the following two reasons. First, the simulation time required for investigation of the initial stage of the nanosecond pulse laser ablation has to be extended beyond 10 ns, which makes large-scale ($\sim 10^8$ atoms) MD simulations computationally expensive. Second, the emergence of lateral density variations and formation of atomic clusters/nanoparticles at the plume–water interface may start before the end of the laser pulse, particularly at laser fluences significantly above the ablation threshold. Under these conditions, a realistic modeling of the laser energy deposition by the tail of the laser pulse should account for the specific absorption characteristics of different components of the ablation plume. The latter requires not only an advanced optical absorption model accounting for the size- and temperature-dependent absorption by plasma, vapor, clusters, and nanoparticles, but also the real-time resolution of the structure of the front part of the ablation plume during the simulation. Leaving the challenge of the design of complete model for laser interaction with heterogeneous multi-component plume to future work, in the present paper we apply small-scale ($\sim 10^6$ atoms) atomistic modeling with a simplified description of the laser energy deposition described in Section 2 for the initial exploration of the changes in the ablation process with an increase in the pulse duration to 1 and 2 ns.

The results of the ns-PLAL simulations are illustrated in Fig. 11 by temperature and density contour plots, which can be

This journal is © the Owner Societies 2020

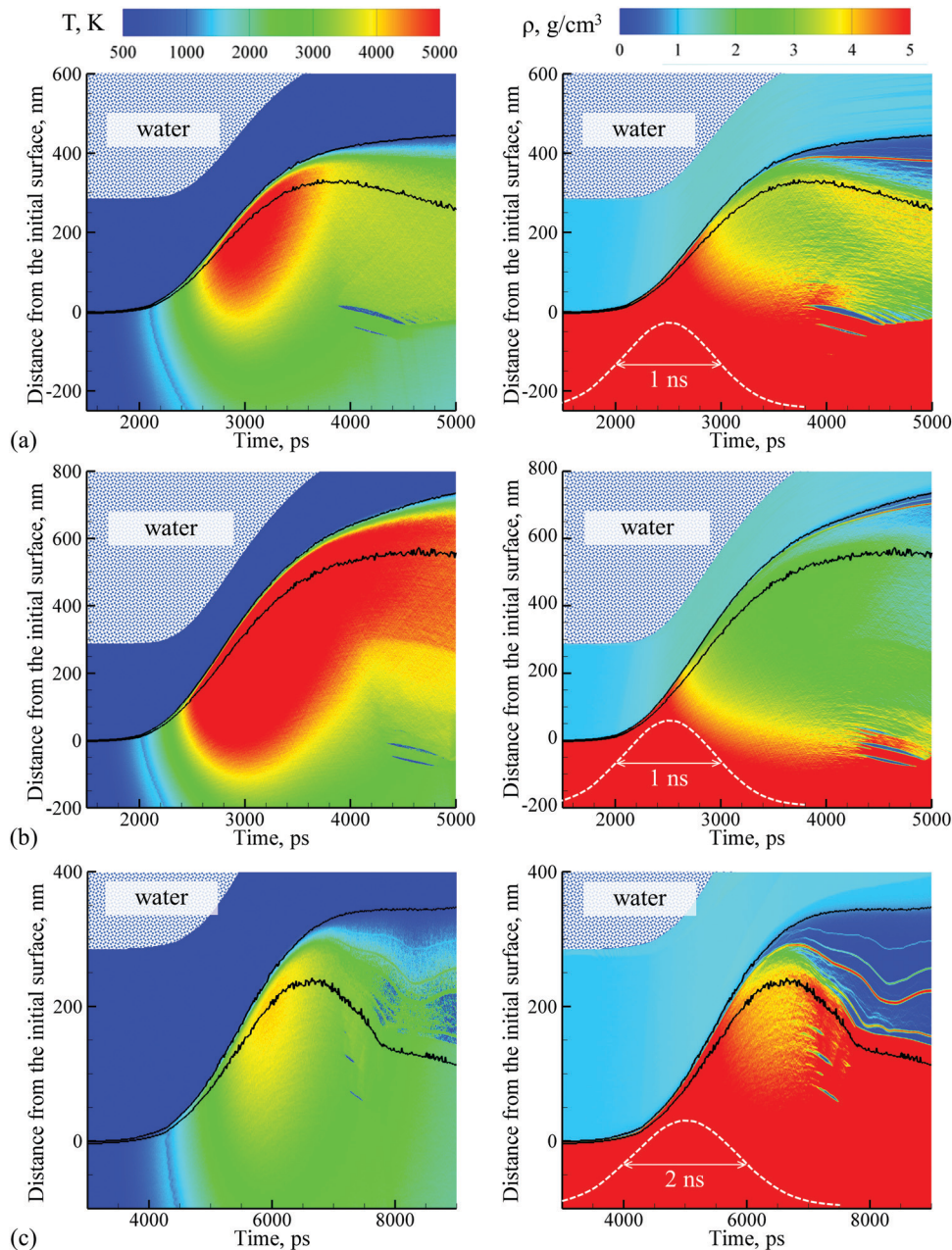*Phys. Chem. Chem. Phys.*, 2020, **22**, 7077–7099 | **7091**

Fig. 11 The temperature (left panels) and density (right panels) contour plots predicted in small-scale simulations of laser ablation of a bulk Ag target irradiated in water by (a) 1 ns laser pulse at an absorbed fluence of 600 mJ cm^{-2}, (b) 1 ns laser pulse at an absorbed fluence of 800 mJ cm^{-2}, and (c) 2 ns laser pulse at an absorbed fluence of 600 mJ cm^{-2}. The blue dotted background represents the implicit presence of water beyond the pressure-transmitting boundary (NRB-w in Fig. 2) applied at the top of the water layer explicitly simulated with coarse-grained MD. The two black lines in each contour plot outline the water–Ag mixing region defined as a region where both water molecules and Ag atoms are present. The temporal shapes of the Gaussian laser pulse are shown in the density contour plots by the white dashed lines.

compared with similar plots shown in Fig. 3 for 400 ps laser pulse. The plots shown in Fig. 11a are for a simulation performed with 1 ns laser pulse at an absorbed fluence of 600 mJ cm^{-2}, *i.e.*, at the same absorbed fluence that is used in the simulation performed with 400 ps pulse and discussed in Sections 3.1 and 3.2. The overall picture of the ablation process, as reflected in the contour plots, is qualitatively similar to that observed for the shorter 400 ps pulse: confined phase explosion of superheated part of the Ag target, appearance and expansion

of a low-density metal–water mixing region, and redeposition of a large part of the ablation plume to the target.

The active expansion of the surface region of the irradiated target starts at about the time when the laser pulse, with Gaussian temporal profile shown in the density contour plots by white dashed line, reaches its maximum and the temperature approaches the critical temperature of Ag. The expanding hot metal pushes the water away from the target and reaches the maximum height of ~390 nm above the initial surface by

7092 | *Phys. Chem. Chem. Phys.*, 2020, **22**, 7077–7099

This journal is © the Owner Societies 2020

~3.9 ns. After that time, a large fraction of the ablation plume reverses the direction of its motion and starts to move back towards the target. A thin transient liquid layer, which shows up as a red line in the density plot, is formed at the plume–water interface due to the effective cooling of the plume front by the water. This layer is analogous to the thicker interfacial layer observed in the simulation performed with 400 ps laser pulse, but is artificially stabilized by the periodic boundary conditions applied to the small computational domain. One can expect that the layer would decompose to individual droplets in a manner similar to that shown in Fig. 6 if a system with larger lateral dimensions would be used in this simulation.

Above the interfacial layer, the superheated water in contact with the plume expands upward and forms a low-density region with thermodynamics conditions favoring rapid nucleation and growth of nanoparticles from the metal vapor rapidly cooled down through the interaction with supercritical water. The nanoparticle formation mechanism in this region is analogous to that discussed above, in Section 3.2, for sub-region R1 identified in the simulation performed with 400 ps laser pulse. Below the interfacial layer, the expansion of the supercritical metal (light blue color in the mixing region of the density contour plots in Fig. 11 corresponds to the values below the critical density of the model Ag material, ρ_c = 2.29 g cm^{-3}) and its mixing with water triggers spontaneous decomposition into a mixture of vapor, atomic clusters, and liquid droplets, in a process analogous to that described in Section 3.2 for sub-region R2.

While the results obtained at the same absorbed fluence with 400 ps and 1 ns laser pulses are similar at the qualitative level, there are some substantial quantitative differences. Due to the slower heating with 1 ns laser pulse, and in the absence of thermal confinement, the maximum lattice temperature reached during the second half of the Gaussian laser pulse is reduced down to ~5000 K (cf., ~8000 K for 400 ps pulse and ~12 000 K for 10 ps pulse at the same absorbed laser fluence). In the absence of the stress confinement, more time allowed for the expansion of the region heated by the longer 1 ns pulse reduces the maximum pressure down to ~2 GPa (cf., ~4.8 GPa for 400 ps pulse and ~38 GPa for 10 ps pulse at the same absorbed laser fluence). The reduced pressure leads to a less vigorous phase explosion and weaker initial push against the water environment, as reflected in the lower maximum height reached by the front of the ablation plume by the end of the plume deceleration stage, ~390 nm in ablation by 1 ns laser pulse, as compared to ~460 nm for 400 ps pulse (Fig. 3a and b) and 550 nm for 10 ps pulse.[8] The lower pressure generated during the ablation process also prevents the compaction of the ablation plume into a thick dense molten layer observed in the simulation performed at 400 ps, Fig. 3b. Instead, the ablation plume is redeposited back to the target in the form of a dense mixture of vapor, atomic clusters and small droplets, as can be seen from the density contour plot shown in Fig. 11a.

In order to compensate for the energy loss through the heat transfer to the bulk of the target during the laser pulse, we also performed a simulation with a pulse duration of 1 ns and an absorbed fluence increased up to 800 mJ cm^{-2}. At this fluence,

the maximum lattice temperature is brought up to the level of ~8000 K (Fig. 11b), similar to that observed at 600 mJ cm^{-2} and pulse duration of 400 ps (Fig. 3a). The maximum pressure, however, increases only moderately, to ~2.5 GPa, and still remains lower than ~4.8 GPa observed in the simulation performed with 400 ps pulse. The increase in temperature results in a more vigorous phase explosion affecting a deeper surface region of the target as compared to the simulation discussed above for the lower absorbed fluence of 600 mJ cm^{-2}. The overall dynamics of the ablation plume expansion and redeposition, however, is similar in the two simulations, and the conditions leading to the three nanoparticle generation mechanisms described in Section 3.2 can be identified in both sets of contour plots shown in Fig. 11a and b.

Finally, to test the effect of further increase of the pulse duration while keeping the same absorbed fluence, we performed an additional simulation at an absorbed fluence of 600 mJ cm^{-2} and a pulse duration of 2 ns. The corresponding temperature and density contour plots are shown in Fig. 11c. The maximum lattice temperature and pressure are reduced with respect to those observed for 1 ns pulse down to ~4000 K and ~1.3 GPa, respectively. The explosive decomposition of the superheated part of the target into vapor, atomic clusters and liquid droplets is suppressed in the largest part of the superheated region by the resistance from the water environment, as can be seen from the density contour plot in Fig. 11c. Most of the material that undergoes the initial expansion and density fluctuations collapses back to the dense molten state by the end of the laser pulse. Only the top part of the target in the immediate contact with water undergoes the explosive phase decomposition. Nevertheless, within this top region, we can still distinguish the characteristic processes of the formation of large droplets at the plume–water interface sandwiched between the overlying colder region, with conditions suitable for nucleation and growth of small nanoparticles, and underlying hot region, with a high density of vapor and liquid droplets emerging from the phase decomposition.

Note that outside the regime of thermal confinement, i.e., for pulse durations longer than ~100 ps in the case of metal targets (see discussion in Section 3.1), the increase of the pulse duration from 400 ps to 1 ns and to 2 ns while keeping the absorbed fluence constant brings the irradiation conditions closer to the ablation threshold fluence, which increases as the square root of the pulse duration $F_{th} \propto \sqrt{\tau_p}$.[71,72] It is not surprising, therefore, that the size of the region undergoing the phase explosion and the extent of the plume expansion at the initial stage of the ablation process are decreasing with increasing pulse duration. One can expect that further increase of the pulse duration at the same absorbed fluence would bring the irradiation conditions below the threshold for the onset of the phase explosion, where the only remaining pathway for the nanoparticle generation would be the evaporation of metal atoms from the target surface into the low-density mixing region followed by nucleation and growth of small nanoparticles.

Overall, the results of the three small-scale PLAL simulations performed with 1 and 2 ns laser pulses suggest that the dynamic picture of the ablation process and the mechanisms

of the nanoparticle formation revealed in the detailed analysis of the simulation performed with 400 ps laser pulse are retained upon the transition to the nanosecond pulses. The quantitative evaluation of the relative efficiency of the nanoparticle production through different mechanisms and the final nanoparticle size distributions in ns-PLAL, however, still requires further investigation.

4. Summary

The results of a large-scale atomistic simulation of PLAL performed with a 400 ps laser pulse, *i.e.*, outside the regimes of stress and thermal confinement, reveal a complex multistep picture of the initial dynamic stage of laser ablation in liquids and uncover several distinct channels of the nanoparticle generation activated during the first nanoseconds of the ablation process. The sequence of dynamic processes predicted in the simulation is illustrated in Fig. 12. The laser energy deposition by the 400 ps pulse occurs simultaneously with the electron–phonon equilibration, melting, and expansion of the heated region in the direction normal to the surface, as well as the diffusional heat transfer to deeper parts of the target (panel 1 in Fig. 12). When the thermodynamic conditions within the molten surface region of the target reach the limit of stability of the superheated liquid, the surface region undergoes an explosive phase decomposition into vapor, atomic clusters, and liquid droplets. The ablation plume produced by the phase explosion of the superheated surface region expands, pushes the overlying water away from the target, but is rapidly decelerated by the water environment, leading to the accumulation of the hot front part of the plume at the interface with water (panel 2 in Fig. 12). A big fraction of the ablation plume is then reflected back and eventually redeposit to the target. At the same time, the water in contact with the hot metal is heated up to the supercritical state, and the expansion of the supercritical water mixed with metal vapor leads to the emergence of a low-density region serving as a precursor of the cavitation bubble (panel 3 in Fig. 12). Rapid deceleration of the plume and cooling of the metal in direct contact with water environment cause roughening of the interfacial layer and its decomposition

into large nanoparticles (panel 4 in Fig. 12), which allows the supercritical water to stream down and mix with a part of the ablation plume retreating towards the target. This interaction triggers a rapid formation of relatively large nanoparticles due to the spinodal decomposition of hot Ag expanding and cooling from the supercritical state (panels 5 and 6 in Fig. 12).

The analysis of the dynamic interaction between the ablation plume and water environment, briefly outlined above, makes it possible to identify three distinct nanoparticle generation mechanisms operating at different stages of the ablation process and in different parts of the emerging cavitation bubble.

(1) First, the formation of a thin transient metal layer at the interface between the ablation plume and water environment followed by the layer decomposition is responsible for the generation of large (diameters above 10 nm) molten nanoparticles at the early stage of the ablation process. The nanoparticles remain in the upper part of the expanding low-density mixing region (cavitation bubble) and are slowly cooled by the interaction with surrounding supercritical water.

(2) Second, at the very front of the emerging cavitation bubble, above the transient interfacial metal layer, a population of small nanoparticles appear through the nucleation and growth from the vapor-phase metal atoms evaporated from the hot interfacial layer into the supercritical water. These small (less than 5 nm) nanoparticles are rapidly cooled to temperatures below the melting temperature and solidify on the timescale of nanoseconds.

(3) Finally, the third and the most numerous group of nanoparticles emerges from the spinodal decomposition of a part of the ablation plume located below the transient interfacial layer. Lower density and higher temperature of the supercritical water in this part of the cavitation bubble create conditions for rapid disappearance of small nanoparticles and predominant growth of larger ones, mostly through the process of collision and coalescence.

The coexistence of the three distinct mechanisms of the nanoparticle generation at the initial stage of the ablation process provides a hint for explaining the origin of broad nanoparticle size distributions commonly observed in nanosecond PLAL experiments. The strong dependence of the nanoparticle cooling and solidification rates on the location within the low-density
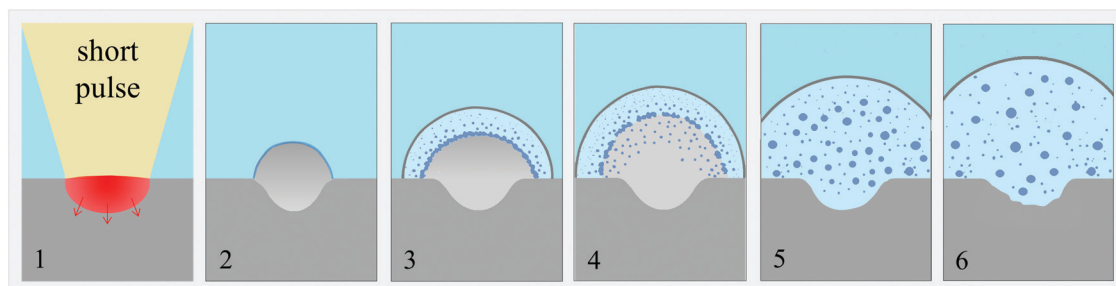
Fig. 12 Schematic illustration of the sequence of dynamic processes triggered by irradiation of a metal target by a *short (hundreds of picoseconds to nanoseconds) laser pulse*. The liquid water is colored blue, the metal target is grey, the ablation plume is light grey, and the expanding cavitation bubble is light blue. The metal nanoparticles and a transient dense metal layer generated at the plume–water interface are shown in dark blue color. The schematic is informed by the atomistic simulations reported in this paper.

7094 | *Phys. Chem. Chem. Phys.*, 2020, **22**, 7077–7099

This journal is © the Owner Societies 2020

metal–water mixing region has important implications for the long-term evolution of the nanoparticle size distribution, as well as for the ability to quench the nanoparticle growth by surface-active agent dissolved in the liquid environment[21,22,68–70] or dope them by adding doping elements to the environment.[73]

The results of smaller-scale simulations performed with 1 and 2 ns laser pulses demonstrate that the general picture of the ablation process and the mechanisms of the nanoparticle formation revealed in the analysis of the simulation performed with 400 ps laser pulse are retained in the nanosecond irradiation regime. The increase of the pulse duration at a fixed absorbed fluence, however, brings the irradiation conditions closer to the ablation threshold, which reduces the amount of the ejected material and the extent of the plume expansion at the initial stage of the ablation process.

The comparison of the results of large-scale simulations performed with short (400 ps – 2 ns, this work) and ultrashort (40 fs – 10 ps, ref. 8 and 40–42) laser pulses makes it possible to elucidate the similarities and differences between the two irradiation regimes. The distinctive characteristics of the dynamics of ultrashort pulse laser ablation, represented schematically in Fig. 1 and discussed in the introduction (Section 1), are related to the conditions of thermal and stress confinement of the deposited laser energy. These conditions result in a more vigorous ablation process, which includes the ejection of relatively cold molten material driven by the dynamic relaxation of laser-induced pressure. As a result, the accumulation of ablated material at the plume–water interface results in the formation of a denser molten layer, which can undergo hydrodynamic instabilities leading to the layer decomposition and injection of some of the large nanoparticles beyond the boundary of the cavitation bubble. With longer (*i.e.*, short rather than ultrashort) laser pulses, the formation of a transient interfacial layer at the plume–water interface is still observed, but the layer is thinner, less dense, and its decomposition produces nanoparticles that all remain within the expanding cavitation bubble. Moreover, a more rarified, loose state of the upper part of the hot metal layer generated at the plume–water interface in the case of short pulse laser ablation facilitates the formation of a large number of nanoparticles through the spinodal decomposition of the ablation plume mixed with supercritical water. The nucleation, growth, and rapid solidification of small nanoparticles at the very front of the emerging cavitation bubble, on the other hand, is a common mechanism observed in simulations of both short and ultrashort pulse laser ablation in water.

Overall, the results of the atomistic simulations performed so far suggest that the initial dynamic stage of the ablation plume interaction with the liquid environment, leading to the formation and decomposition of a dense hot metal layer at the plume–liquid interface, is playing an important role in the nanoparticle generation. The fundamental difference between short and ultrashort pulse laser ablation in liquids is mainly related to the differences in the characteristics of this interfacial layer and its interaction with liquid environment. Note that the reported simulations are performed at laser fluences that are relatively close to (a few times higher than) the threshold values for the ablation onset. Further increase of the laser fluence may substantially alter the characteristics of PLAL, particularly for nanosecond pulses, where the plasma shielding and scattering of the tail of the laser pulse could play a significant role. These effects, along with the sensitivity of the mechanisms of nanoparticle generation to properties of the liquid environment, still await detailed computational exploration.

Conflicts of interest

There are no conflicts of interest to declare.

Appendix: phase diagram and surface tension of the model EAM Ag

The interpretation of the results of the simulations performed with a semi-empirical EAM potential[60] describing the interatomic interactions among Ag atoms requires a clear understanding of the thermodynamic properties of the model material. In particular, the information on the liquid–vapor binodal curves and the temperature dependence of the liquid–vapor interfacial tension is needed for analysis of the conditions for condensation and evaporation of nanoparticles performed in Section 3.2.

In this work, the high-temperature thermodynamic properties of the model EAM Ag material are evaluated in a series of small-scale liquid–vapor coexistence simulations performed for a system containing 8000 atoms. The simulations are performed with periodic boundary conditions applied in all three directions. The computational system is initially equilibrated in the liquid state at the equilibrium melting point. The system is then extended along one dimension to 35 nm (or to 40 nm for the four data points closest to the thermodynamic critical point) to create an empty space for the vapor formation. During the following 375 ps, the system is slowly heated to a target temperature, leading to the formation of a system with two liquid–vapor interfaces perpendicular to the direction in which the system is elongated. For each target temperature, the simulation is then continued for another 5 ns under constant-volume and constant-temperature conditions, and the data acquisition is performed. The density profile is produced by dividing the system into 0.1 Å bins and averaging over the number of atoms found in each bin at each MD timestep.

The equilibrium values of liquid and vapor densities found in the MD simulations are used to fit parts of the binodal curves away from the immediate vicinity of the critical point, shown by black curves in Fig. 13a. In the vicinity of the critical point, the data generated in MD simulations is fitted to the equations predicted from the renormalization group theory[74,75] (green and red curves in Fig. 13a). The result of this fitting allows us to deduce the values of critical temperature and density, $T_c = 3360$ K and $n_c = 12.77$ atoms per nm^3 ($\rho_c = 2.29$ g cm^{-3}). An independent simulation performed at the critical point gives the values of the critical pressure of 35 MPa.

While the theoretical equations based on the renormalization group theory[74,75] can accurately describe the coexistence
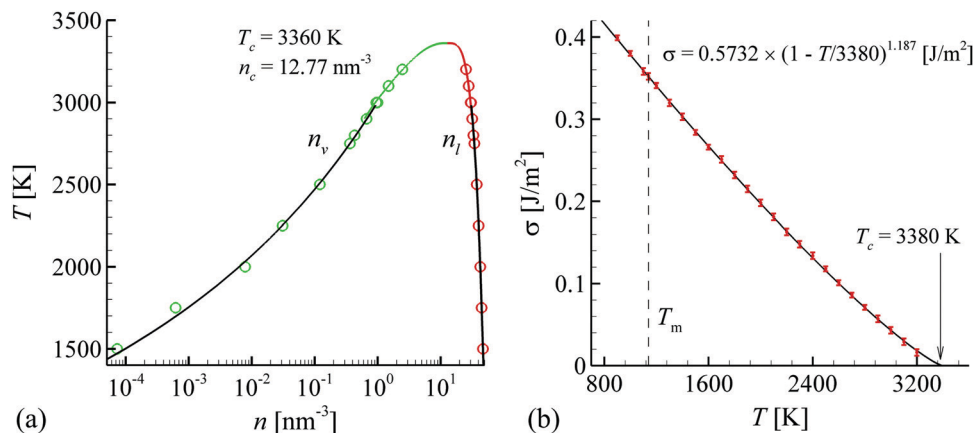
Fig. 13 The temperature–density (T–n) plane of the liquid–vapor part of the phase diagram (a) and the temperature dependence of surface tension (b) calculated for the model EAM Ag used in the simulations of PLAL reported in this paper. In (a), the black curves are the parts of the binodal curves obtained by direct fitting to the results of liquid–vapor coexistence simulations shown by green and red points; the red and green curves represent the fitting of the data points to the dependences predicted from renormalization group theory for the material behavior near the critical point.[74,75] The critical density $n_c = 12.77$ nm^{-3} obtained from the fitting, corresponds to $\rho_c = 2.29$ g cm^{-3}. In (b) the error bar corresponds to the standard error.

curves near the critical point, at lower temperatures the curve for the vapor density predicted by the corresponding equation deviates from points computed in MD simulations. Therefore, the purely empirical fits to the data points, shown by black lines in Fig. 13a, are used in the evaluation of the critical size for nanoparticle growth through condensation in Section 3.2.

The evaluation of the critical nanoparticle size for condensation given by eqn (1) also requires knowledge of the temperature dependence of the liquid–vapor interfacial tension. The interfacial tension is evaluated in MD simulations, similar to those described above, using the test area method.[76] Symmetric fluctuations are utilized, and the fluctuation magnitude is chosen to be 2×10^{-4}. The temperature dependence of the interfacial tension is fitted to a semiempirical equation[77] $\sigma = \sigma_0(1 - T/T_c)^\mu$, as shown in Fig. 13b. The fitting to this equation also enables an independent determination of the critical temperature, which yields a value of $T_c = 3380$ K, close to the one predicted from the fitting of the binodal curves to theoretical equations in Fig. 13a.

Acknowledgements

References

1 D. Amans, W. Cai and S. Barcikowski, Status and demand of research to bring laser generation of nanoparticles in liquids to maturity, *Appl. Surf. Sci.*, 2019, **488**, 445–454.

2 D. Zhang, B. Gökce and S. Barcikowski, Laser synthesis and processing of colloids: Fundamentals and applications, *Chem. Rev.*, 2017, **117**, 3990–4103.

3 A. Kanitz, M.-R. Kalus, E. L. Gurevich, A. Ostendorf, S. Barcikowski and D. Amans, Review on experimental and theoretical investigations of the early stage, femtoseconds to microseconds processes during laser ablation in liquid-phase for the synthesis of colloidal nanoparticles, *Plasma Sources Sci. Technol.*, 2019, **28**, 103001.

4 S. Barcikowski, A. Plech, K. S. Suslick and A. Vogel, Materials synthesis in a bubble, *MRS Bull.*, 2019, **44**, 382–391.

5 J. Lam, J. Lombard, C. Dujardin, G. Ledoux, S. Merabia and D. Amans, Dynamical study of bubble expansion following laser ablation in liquids, *Appl. Phys. Lett.*, 2016, **108**, 074104.

6 S. Ibrahimkutty, P. Wagener, T. d. S. Rolo, D. Karpov, A. Menzel, T. Baumbach, S. Barcikowski and A. Plech, A hierarchical view on material formation during pulsed-laser synthesis of nanoparticles in liquid, *Sci. Rep.*, 2015, **5**, 16313.

7 J. Tomko, J. J. Naddeo, R. Jimenez, Y. Tan, M. Steiner, J. M. Fitz-Gerald, D. M. Bubb and S. M. O'Malley, Size and polydispersity trends found in gold nanoparticles synthesized by laser ablation in liquids, *Phys. Chem. Chem. Phys.*, 2015, **17**, 16327–16333.

8 C.-Y. Shih, R. Streubel, J. Heberle, A. Letzel, M. V. Shugaev, C. Wu, M. Schmidt, B. Gökce, S. Barcikowski and L. V. Zhigilei, Two mechanisms of nanoparticle generation in picosecond laser ablation in liquids: the origin of the bimodal size distribution, *Nanoscale*, 2018, **10**, 6900–6910.

9 W. Charee and V. Tangwarodomnukun, Dynamic features of bubble induced by a nanosecond pulse laser in still and flowing water, *Opt. Laser Technol.*, 2018, **100**, 230–243.

10 T. Tsuji, Y. Tsuboi, N. Kitamura and M. Tsuji, Microsecond-resolved imaging of laser ablation at solid–liquid interface: investigation of formation process of nano-size metal colloids, *Appl. Surf. Sci.*, 2004, **229**, 365–371.

7096 | *Phys. Chem. Chem. Phys.*, 2020, **22**, 7077–7099

This journal is © the Owner Societies 2020

11 T. Tsuji, Y. Okazaki, Y. Tsuboi and M. Tsuji, Nanosecond time-resolved observations of laser ablation of silver in water, *Jpn. J. Appl. Phys.*, 2007, **46**, 1533–1535.

12 S. Barcikowski, A. Menéndez-Manjón, B. Chichkov, M. Brikas and G. Raciukaitis, Generation of nanoparticle colloids by picosecond and femtosecond laser ablations in liquid flow, *Appl. Phys. Lett.*, 2007, **91**, 083113.

13 D. Riabinina, M. Chaker and J. Margot, Dependence of gold nanoparticle production on pulse duration by laser ablation in liquid media, *Nanotechnology*, 2012, **23**, 135603.

14 A. De Bonis, A. Galasso, A. Santagata and R. Teghil, Laser ablation of GaAs in liquid: the role of laser pulse duration, *J. Phys. D: Appl. Phys.*, 2016, **49**, 035301.

15 A. Hamad, L. Li and Z. Liu, A comparison of the characteristics of nanosecond, picosecond and femtosecond lasers generated Ag, TiO_2 and Au nanoparticles in deionised water, *Appl. Phys. A: Mater. Sci. Process.*, 2015, **120**, 1247–1260.

16 P. A. Danilov, A. A. Ionin, S. I. Kudryashov, A. A. Rudenko, I. N. Saraeva and D. A. Zayarny, Non-monotonic variation of Au nanoparticle yield during femtosecond/picosecond laser ablation in water, *Laser Phys. Lett.*, 2017, **14**, 056001.

17 D. S. Ivanov, T. Izgin, A. N. Maiorov, V. P. Veiko, B. Rethfeld, Y. I. Dombrovska, M. E. Garcia, I. N. Zavestovskaya, S. M. Klimentov and A. V. Kabashin, Numerical investigation of ultrashort laser-ablative synthesis of metal nanoparticles in liquids using the atomistic-continuum model, *Molecules*, 2020, **25**, 67.

18 R. Streubel, G. Bendt and B. Gökce, Pilot-scale synthesis of metal nanoparticles by high-speed pulsed laser ablation in liquids, *Nanotechnology*, 2016, **27**, 205602.

19 S. Reich, A. Letzel, A. Menzel, N. Kretzschmar, B. Gökce, S. Barcikowski and A. Plech, Early appearance of crystalline nanoparticles in pulsed laser ablation in liquids dynamics, *Nanoscale*, 2019, **11**, 6962–6969.

20 S. Ibrahimkutty, P. Wagener, A. Menzel, A. Plech and S. Barcikowski, Nanoparticle formation in a cavitation bubble after pulsed laser ablation in liquid studied with high time resolution small angle X-ray scattering, *Appl. Phys. Lett.*, 2012, **101**, 103104.

21 A. Letzel, B. Gökce, P. Wagener, S. Ibrahimkutty, A. Menzel, A. Plech and S. Barcikowski, Size quenching during laser synthesis of colloids happens already in the vapor phase of the cavitation bubble, *J. Phys. Chem. C*, 2017, **121**, 5356–5365.

22 A. Letzel, S. Reich, T. dos Santos Rolo, A. Kanitz, J. Hoppius, A. Rack, M. P. Olbinado, A. Ostendorf, B. Gökce, A. Plech and S. Barcikowski, Time and mechanism of nanoparticle functionalization by macromolecular ligands during pulsed laser ablation in liquids, *Langmuir*, 2019, **35**, 3038–3047.

23 P. Wagener, S. Ibrahimkutty, A. Menzel, A. Plech and S. Barcikowski, Dynamics of silver nanoparticle formation and agglomeration inside the cavitation bubble after pulsed laser ablation in liquid, *Phys. Chem. Chem. Phys.*, 2013, **15**, 3068–3074.

24 W. T. Nichols, T. Sasaki and N. Koshizaki, Laser ablation of a platinum target in water. I. Ablation mechanisms, *J. Appl. Phys.*, 2006, **100**, 114911.

25 W. T. Nichols, T. Sasaki and N. Koshizaki, Laser ablation of a platinum target in water. II. Ablation rate and nanoparticle size distributions, *J. Appl. Phys.*, 2006, **100**, 114912.

26 N. Lasemi, U. Pacher, L. V. Zhigilei, O. Bomatí-Miguel, R. Lahoz and W. Kautek, Pulsed laser ablation and incubation of nickel, iron and tungsten in liquids and air, *Appl. Surf. Sci.*, 2018, **433**, 772–779.

27 A. Miotello and R. Kelly, Laser-induced phase explosion: new physical problems when a condensed phase approaches the thermodynamic critical temperature, *Appl. Phys. A: Mater. Sci. Process.*, 1999, **69**, S67–S73.

28 L. V. Zhigilei and B. J. Garrison, Microscopic mechanisms of laser ablation of organic solids in the thermal and stress confinement irradiation regimes, *J. Appl. Phys.*, 2000, **88**, 1281–1298.

29 N. M. Bulgakova and A. V. Bulgakov, Pulsed laser ablation of solids: transition from normal vaporization to phase explosion, *Appl. Phys. A: Mater. Sci. Process.*, 2001, **73**, 199–208.

30 L. V. Zhigilei, Z. Lin and D. S. Ivanov, Atomistic modeling of short pulse laser ablation of metals: Connections between melting, spallation, and phase explosion, *J. Phys. Chem. C*, 2009, **113**, 11892–11906.

31 L. V. Zhigilei, Dynamics of the plume formation and parameters of the ejected clusters in short-pulse laser ablation, *Appl. Phys. A: Mater. Sci. Process.*, 2003, **76**, 339–350.

32 C. Wu and L. V. Zhigilei, Microscopic mechanisms of laser spallation and ablation of metal targets from large-scale molecular dynamics simulations, *Appl. Phys. A: Mater. Sci. Process.*, 2014, **114**, 11–32.

33 G. Paltauf and P. E. Dyer, Photomechanical processes and effects in ablation, *Chem. Rev.*, 2003, **103**, 487–518.

34 E. Leveugle, D. S. Ivanov and L. V. Zhigilei, Photomechanical spallation of molecular and metal targets: molecular dynamics study, *Appl. Phys. A: Mater. Sci. Process.*, 2004, **79**, 1643–1655.

35 M. V. Shugaev and L. V. Zhigilei, Thermodynamic analysis and atomistic modeling of subsurface cavitation in photomechanical spallation, *Comput. Mater. Sci.*, 2019, **166**, 311–317.

36 K. Nahen and A. Vogel, Plume dynamics and shielding by the ablation plume during Er:YAG laser ablation, *J. Biomed. Opt.*, 2002, **7**, 165–178.

37 C. Zhao, Q. Guo, X. Li, N. Parab, K. Fezzaa, W. Tan, L. Chen and T. Sun, Bulk-explosion-induced metal spattering during laser processing, *Phys. Rev. X*, 2019, **9**, 021052.

38 T. D. Bennett, C. P. Grigoropoulos and D. J. Krajnovich, Near-threshold laser sputtering of gold, *J. Appl. Phys.*, 1995, **77**, 849–864.

39 A. N. Volkov and L. V. Zhigilei, Melt dynamics and melt-through time in continuous wave laser heating of metal films: Contributions of the recoil vapor pressure and Marangoni effects, *Int. J. Heat Mass Transfer*, 2017, **112**, 300–317.

40 C.-Y. Shih, C. Wu, M. V. Shugaev and L. V. Zhigilei, Atomistic modeling of nanoparticle generation in short pulse laser ablation of thin metal films in water, *J. Colloid Interface Sci.*, 2017, **489**, 3–17.

This journal is © the Owner Societies 2020

Phys. Chem. Chem. Phys., 2020, **22**, 7077–7099 | 7097

41 C.-Y. Shih, M. V. Shugaev, C. Wu and L. V. Zhigilei, Generation of subsurface voids, incubation effect, and formation of nanoparticles in short pulse laser interactions with bulk metal targets in liquid: Molecular dynamics study, *J. Phys. Chem. C*, 2017, **121**, 16549–16567.

42 C.-Y. Shih, I. Gnilitskyi, M. V. Shugaev, E. Skoulas, E. Stratakis and L. V. Zhigilei, Effect of liquid environment on single-pulse generation of laser induced periodic surface structures and nanoparticles, *Nanoscale*, 2020, DOI: 10.1039/D0NR00269K.

43 H. J. Kull, Theory of the Rayleigh-Taylor instability, *Phys. Rep.*, 1991, **206**, 197–325.

44 M. Brouillette, The Richtmyer–Meshkov instability, *Annu. Rev. Fluid Mech.*, 2002, **34**, 445–468.

45 A. V. Kabashin and M. Meunier, Synthesis of colloidal nanoparticles during femtosecond laser ablation of gold in water, *J. Appl. Phys.*, 2003, **94**, 7941–7943.

46 J.-P. Sylvestre, A. V. Kabashin, E. Sacher and M. Meunier, Femtosecond laser ablation of gold in water: influence of the laser-produced plasma on the nanoparticle size distribution, *Appl. Phys. A: Mater. Sci. Process.*, 2005, **80**, 753–758.

47 L. Gamrad, C. Rehbock, J. Krawinkel, B. Tumursukh, A. Heisterkamp and S. Barcikowski, Charge balancing of model gold-nanoparticle-peptide conjugates controlled by the peptide's net charge and the ligand to nanoparticle ratio, *J. Phys. Chem. C*, 2014, **118**, 10302–10313.

48 G. Marzun, J. Nakamura, X. Zhang, S. Barcikowski and P. Wagener, Size control and supporting of palladium nanoparticles made by laser ablation in saline solution as a facile route to heterogeneous catalysts, *Appl. Surf. Sci.*, 2015, **348**, 75–84.

49 C. Rehbock, J. Jakobi, L. Gamrad, S. van der Meer, D. Tiedemann, U. Taylor, W. Kues, D. Rath and S. Barcikowski, Current state of laser synthesis of metal and alloy nanoparticles as ligand-free reference materials for nano-toxicological assays, *Beilstein J. Nanotechnol.*, 2014, **5**, 1523–1541.

50 T. Tsuji, T. Kakita and M. Tsuji, Preparation of nano-size particles of silver with femtosecond laser ablation in water, *Appl. Surf. Sci.*, 2003, **206**, 314–320.

51 G. Cristoforetti, E. Pitzalis, R. Spiniello, R. Ishak and M. Muniz-Mirand, Production of palladium nanoparticles by pulsed laser ablation in water and their characterization, *J. Phys. Chem. C*, 2011, **115**, 5073–5083.

52 G. Marzun, C. Streich, S. Jendrzej, S. Barcikowski and P. Wagener, Adsorption of colloidal platinum nanoparticles to supports: Charge transfer and effects of electrostatic and steric interactions, *Langmuir*, 2014, **30**, 11928–11936.

53 D. S. Ivanov and L. V. Zhigilei, Combined atomistic-continuum modeling of short-pulse laser melting and disintegration of metal films, *Phys. Rev. B: Condens. Matter Mater. Phys.*, 2003, **68**, 064114.

54 C. Wu, M. S. Christensen, J.-M. Savolainen, P. Balling and L. V. Zhigilei, Generation of sub-surface voids and a nano-crystalline surface layer in femtosecond laser irradiation of a single crystal Ag target, *Phys. Rev. B: Condens. Matter Mater. Phys.*, 2015, **91**, 035413.

55 M. Tabetah, A. Matei, C. Constantinescu, N. P. Mortensen, M. Dinescu, J. Schou and L. V. Zhigilei, The minimum amount of ''matrix'' needed for matrix-assisted pulsed laser deposition of biomolecules, *J. Phys. Chem. B*, 2014, **118**, 13290–13299.

56 J. Zou, C. Wu, W. D. Robertson, L. V. Zhigilei and R. J. D. Miller, Molecular dynamics investigation of desorption and ion separation following picosecond infrared laser (PIRL) ablation of an ionic aqueous protein solution, *J. Chem. Phys.*, 2016, **145**, 204202.

57 E. T. Karim, M. V. Shugaev, C. Wu, Z. Lin, R. F. Hainsey and L. V. Zhigilei, Atomistic simulation study of short pulse laser interactions with a metal target under conditions of spatial confinement by a transparent overlayer, *J. Appl. Phys.*, 2014, **115**, 183501.

58 S. I. Anisimov, B. L. Kapeliovich and T. L. Perel'man, Electron emission from metal surfaces exposed to ultra-short laser pulses, *Sov. Phys. – JETP*, 1974, **39**, 375–377.

59 Z. Lin, L. V. Zhigilei and V. Celli, Electron-phonon coupling and electron heat capacity of metals under conditions of strong electron-phonon nonequilibrium, *Phys. Rev. B: Condens. Matter Mater. Phys.*, 2008, **77**, 075133.

60 S. M. Foiles, M. I. Baskes and M. S. Daw, Embedded-atom-method functions for the fcc metals Cu, Ag, Au, Ni, Pd, Pt, and their alloys, *Phys. Rev. B: Condens. Matter Mater. Phys.*, 1986, **33**, 7983–7991.

61 S. M. Foiles and J. B. Adams, Thermodynamic properties of FCC transition metals as calculated with the embedded-atom method, *Phys. Rev. B: Condens. Matter Mater. Phys.*, 1989, **40**, 5909–5915.

62 C. Wu, D. A. Thomas, Z. Lin and L. V. Zhigilei, Runaway lattice-mismatched interface in an atomistic simulation of femtosecond laser irradiation of Ag film–Cu substrate system, *Appl. Phys. A: Mater. Sci. Process.*, 2011, **104**, 781–792.

63 *Handbook of Chemistry and Physics*, ed. R. C. Weast, CRC Press, Boca Raton, 64th edn, 1983.

64 A. Naghilou, M. He, J. S. Schubert, L. V. Zhigilei and W. Kautek, Femtosecond laser generation of microbumps and nanojets on single and bilayer Cu/Ag thin films, *Phys. Chem. Chem. Phys.*, 2019, **21**, 11846–11860.

65 M. E. Povarnitsyn, T. E. Itina, P. R. Levashov and K. V. Khishchenko, Mechanisms of nanoparticle formation by ultra-short laser ablation of metals in liquid environment, *Phys. Chem. Chem. Phys.*, 2013, **15**, 3108–3114.

66 M. E. Povarnitsyn and T. E. Itina, Hydrodynamic modeling of femtosecond laser ablation of metals in vacuum and in liquid, *Appl. Phys. A: Mater. Sci. Process.*, 2014, **117**, 175–178.

67 W. Thomson, On the equilibrium of vapour at a curved surface of liquid, *Philos. Mag.*, 1871, **42**, 448–452.

68 F. Mafuné, J.-y. Kohno, Y. Takeda, T. Kondow and H. Sawabe, Formation and size control of silver nanoparticles by laser ablation in aqueous solution, *J. Phys. Chem. B*, 2000, **104**, 9111–9117.

69 J.-P. Sylvestre, S. Poulin, A. V. Kabashin, E. Sacher, M. Meunier and J. H. T. Luong, Surface chemistry of gold

7098 | *Phys. Chem. Chem. Phys.*, 2020, **22**, 7077–7099

This journal is © the Owner Societies 2020

nanoparticles produced by laser ablation in aqueous media, *J. Phys. Chem. B*, 2004, **108**, 16864–16869.

70 T. Tsuji, D.-H. Thang, Y. Okazaki, M. Nakanishi, Y. Tsuboi and M. Tsuji, Preparation of silver nanoparticles by laser ablation in polyvinylpyrrolidone solutions, *Appl. Surf. Sci.*, 2008, **254**, 5224–5230.

71 B. N. Chichkov, C. Momma, S. Nolte, F. von Alvensleben and A. Tünnermann, Femtosecond, picosecond and nanosecond laser ablation of solids, *Appl. Phys. A: Mater. Sci. Process.*, 1996, **63**, 109–115.

72 N. Arnold, B. Luk'yanchuk and N. Bityurin, A fast quantitative modelling of ns laser ablation based on non-stationary averaging technique, *Appl. Surf. Sci.*, 1998, **127–129**, 184–192.

73 A. Chemin, J. Lam, G. Laurens, F. Trichard, V. Motto-Ros, G. Ledoux, V. Jarý, V. Laguta, M. Nikl, C. Dujardin and D. Amans, Doping nanoparticles using pulsed laser ablation in a liquid containing the doping agent, *Nanoscale Adv.*, 2019, **1**, 3963–3972.

74 H. Okumura and F. Yonezawa, Liquid–vapor coexistence curves of several interatomic model potentials, *J. Chem. Phys.*, 2000, **113**, 9162–9168.

75 H. Okumura and F. Yonezawa, Reliable determination of the liquid–vapor critical point by the *NVT* plus test particle method, *J. Phys. Soc. Jpn.*, 2001, **70**, 1990–1994.

76 G. J. Gloora and G. Jackson, Test-area simulation method for the direct determination of the interfacial tension of systems with continuous or discontinuous potentials, *J. Chem. Phys.*, 2005, **123**, 134703.

77 J. M. Howe, *Interfaces in Materials: Atomic Structure, Thermodynamics and Kinetics of Solid–Vapor, Solid–Liquid and Solid–Solid Interfaces*, Wiley, New York, 1997.

This journal is © the Owner Societies 2020

Phys. Chem. Chem. Phys., 2020, **22**, 7077–7099 | **7099**